

Article

Provenance of Volcanogenic Deposits from the Shanxi Formation of the Daniudi Gas Field, Ordos Basin, and Its Tectonic Implications

Xuejiao Qu ¹ , Qiao Wang ¹, Dunfan Wang ^{1,*}, Tao Lei ², Hao Chen ^{3,4}, Jia Wang ¹, Wei Jiang ¹, Wei Zhang ¹, Long Luo ¹, Jianping Liu ¹, Nan Jiang ^{1,5}, Xuanbo Gao ¹ and Xianfeng Tan ¹

- ¹ School of Petroleum Engineering, Chongqing University of Science and Technology, Chongqing 401331, China; quxuejiao2008@aliyun.com (X.Q.); 2021201203@cqust.edu.cn (Q.W.); 2012915@cqust.edu.cn (J.W.); 2023037@cqust.edu.cn (W.J.); 2022201115@cqust.edu.cn (W.Z.); 2019035@cqust.edu.cn (L.L.); 2022022@cqust.edu.cn (J.L.); 2016909@cqust.edu.cn (N.J.); 2017022@cqust.edu.cn (X.G.); xianfengtian8299@163.com (X.T.)
- ² Exploration and Development Research Institute of North China Branch Company, SINOPEC, Zhengzhou 450006, China; leitao.hbsj@sinopec.com
- ³ Chongqing 208 Geoenvironmental Engineering Survey and Design Institute Co., Ltd., Chongqing 401121, China; 2022201086@cqust.edu.cn
- ⁴ College of Earth Sciences, Chengdu University of Technology, Chengdu 610059, China
- ⁵ School of Geoscience and Technology, Southwest Petroleum University, Chengdu 610500, China
- * Correspondence: 2023201018@cqust.edu.cn

Abstract: Through detailed drill-core description, petrography, cathodoluminescence imaging, and geochemistry analysis, sedimentary deposits with a high content of volcanogenic components (27.6%) were discovered in the Shanxi Formation of the Daniudi Gas Field, Ordos Basin. The volcanogenic components include volcanogenic quartz, lava fragments (dominated by rhyolite fragments), tuff fragments, and tuffaceous matrix. In addition, at least two volcanic ash layers were discovered. Although the metamorphic rocks of the Precambrian succession in the ancient land of Yin Mountain are usually considered the primary source of the Shanxi formation, it is most likely that the volcanogenic components were derived from intermediate-acid volcanic materials that accumulated in the Daqingshan area during the Late Carboniferous to Early Permian. Those volcanogenic components are mainly transported by flowing water rather than by air from origin to basin. In addition, the accumulation of volcanic materials in the Daqingshan area was controlled by volcanic eruptions occurring solely in this area, rather than by the Inner Mongolia Orogenic Belt. Those volcanic eruptions were related to the southward subduction of the Paleo-Asian Ocean Plate beneath the northern margin of the North China Plate in the Late Carboniferous to Early Permian. The active continental margin related to the subduction of the Paleo-Asian Ocean Plate lasted at least until the Early Permian, and the closure of the Paleo-Asian Ocean must have occurred later than the Early Permian.

Keywords: volcanogenic sedimentary deposits; provenance; tectonic evolution; Shanxi formation; Ordos Basin



Citation: Qu, X.; Wang, Q.; Wang, D.; Lei, T.; Chen, H.; Wang, J.; Jiang, W.; Zhang, W.; Luo, L.; Liu, J.; et al. Provenance of Volcanogenic Deposits from the Shanxi Formation of the Daniudi Gas Field, Ordos Basin, and Its Tectonic Implications. *Minerals* **2023**, *13*, 1546. <https://doi.org/10.3390/min13121546>

Academic Editors: Georgia Pe-Piper and Manuel Francisco Pereira

Received: 3 October 2023

Revised: 6 December 2023

Accepted: 11 December 2023

Published: 14 December 2023



Copyright: © 2023 by the authors. Licensee MDPI, Basel, Switzerland. This article is an open access article distributed under the terms and conditions of the Creative Commons Attribution (CC BY) license (<https://creativecommons.org/licenses/by/4.0/>).

1. Introduction

The Ordos Basin is a huge intracratonic basin located in the western margin of the North China Plate, spanning 28×10^4 km² (Figure 1a) [1,2]. It is bordered to the north by the Xing-Meng Orogenic Belt (Figure 1b) [3,4], which has experienced multi-stage oceanic plate subduction, crustal accretion, and multi-block amalgamation between the North China Plate, the Paleo-Asian Ocean Plate, and the southern part of the Siberia Plate since the Early Paleozoic [5–8]. During the Shanxi Formation stage (Early Permian), continental clastic rocks accumulated in the north of the basin as the result of intense tectonic activity in the Xing-Meng Orogenic Belt [9–13]. However, petrographic data on sandstones deposited

in intracratonic or epicratonic basins provide noteworthy information about provenance composition and geotectonic setting [14–20]. The continental clastic rocks of the Shanxi Formation in the Daniudi Gas Field, located in the north of the Ordos Basin, can help us better understand the lithology, age of provenance, and tectonic evolution of the Xing-Meng Orogenic Belt.

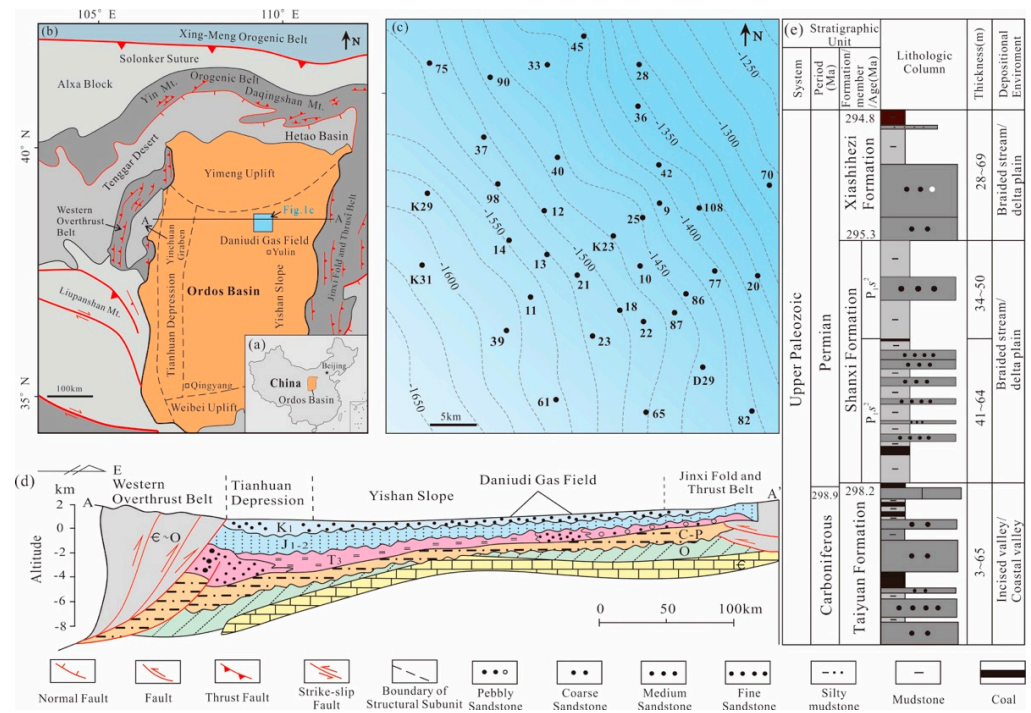


Figure 1. Location map and subtectonic units of the Ordos Basin and the Shanxi Formation stratigraphy. (a) Location of the Ordos Basin, China; (b) locality map of the Daniudi Gas Field, showing the distribution of the main depressions and uplifts within and surrounding the Ordos Basin (modified from Darby & Ritts (2002) [21] and Xu et al. (2017) [22]); (c) sampling well locations in the Daniudi Gas Field; (d) geologic structure cross section of the Ordos Basin (modified from Yang et al. (2005) [23]); (e) Upper Paleozoic stratigraphy for the region around the Daniudi Gas Field. The stratigraphic ages refer to Shen et al., 2022 and Cohen et al., 2023 [24,25].

Previous researchers have documented that the provenance of the Shanxi Formation in the Daniudi Gas Field was attributed to active recycled-orogenic provenance, and the source rock derived from metamorphic rock of Precambrian succession in the ancient land of Yin Mountain in the north of the Ordos Basin, and mixed with granite and alkaline basalt [9,10,12,13,26]. However, the high content of volcanogenic components (average over 27.6%) discovered recently in the Shanxi Formation has raised questions that previous research could not fully address. Their characteristics, provenance, and transportation have not been thoroughly analyzed. Furthermore, these volcanogenic components hold essential clues for understanding the evolution of the Xing-Meng Orogenic Belt and the closure of the Paleo-Asian Ocean, especially the debated subduction direction of the plate in the Xing-Meng Orogenic Belt and the closure period of the Paleo-Asian Ocean [27–41].

In this work, we carried out a comprehensive study on the Shanxi Formation in the Daniudi Gas Field through core observation, thin section fine identification, scanning electron microscope (SEM) analysis, and cathodoluminescence (CL) images analysis to determine the detail types and contents of volcanogenic components. Furthermore, we integrated the geochemical data obtained from fine-grained rocks with previous achievements. This allowed us to utilize petrographic data for characterizing the provenance and transport processes of the volcanogenic components. Additionally, the subduction direction of the

plate in the Xing-Meng Orogenic Belt during the Late Carboniferous to Early Permian and the closure period of the Paleo-Asian Ocean were discussed.

2. Geological Setting

The Ordos Basin is a cratonic basin with multiple tectonic systems, multicyclic evolution, and various sediment types [42–44]. It developed on a basement of Archean granulites and Lower Proterozoic greenschists of the North China Block [23]. The basement is overlain by sedimentary rocks of the Proterozoic Changcheng (Pt_2ch), Jixian (Pt_2jx), and Sinian (Pt_2z) systems. The Upper Carboniferous was directly deposited upon the Cambrian and Ordovician strata, with a ~130 Ma discontinuity between the Late Ordovician and Carboniferous periods [45–48]. The Mesozoic record is more complete and is interrupted only by Lower and Upper Jurassic lacunas [49]. The Paleozoic tectonic evolution of the northern part of the North China Plate (including the Ordos Basin) is thought to have been deeply influenced by the evolution of the closure of the Paleo-Asian Ocean [6,50,51]. Deposition and magmatism records show that the North China Plate remained stable during the Early Paleozoic, and its northern part was a passive continental margin [52,53]. The Bainaimiao Island Arc developed between the North China Plate and the Paleo-Asian Ocean, which was triggered by the northward subduction of the South Bainaimiao Ocean at 520~420 Ma [53,54]. In the Late Silurian to Early Devonian, the northern part of the North China Plate changed to an active continental margin due to the arc-continent collision between the North China Plate and the Bainaimiao Island Arc [31,52,55]. Since the latest Early Carboniferous to Early Permian, the northern margin of the North China Plate evolved into an Andean-style active continental margin with volcanic arc and the Paleo-uplift of Inner Mongolia [31,54,56]. At the same time, volcanic eruptions of continental arc widely developed in the Inner Mongolia Paleo-uplift, and basalt, basaltic andesite, andesite, dacite, rhyolite, tuff, and tuffaceous sandstone accumulated in the Paleo-uplift [3,57,58]. But most of the volcanic rocks were denuded after a strong exhumation [59]. The tuff layers in the Late Carboniferous to Permian sedimentary basins (including the Ordos Basin) in the northern part of the North China Plate may have recorded those volcanic eruptions [60,61]. In the Late Permian to early Triassic, the Paleo-Asian Ocean finally closed along the Solonker Suture Zone, which resulted in a collisional orogeny between the northern margin of the North China Plate and the southern accretionary continental margin of the Siberia Plate [3,6,30,52,62–64]. Magmatism and crustal accretion associated with post-orogenic extension developed in this area along with the collision and suturing [53,65].

The Ordos Basin can be subdivided into six structural units: the Western Overthrust Belt, the Tianhuan Depression, the Yishan Ramp, the Jinxi Fold and Thrust Belt, the Yimeng Uplift, and the Weibei Uplift [66–71] (Figure 1b). The Daniudi Gas Field is situated in the northern part of the Yishan Ramp and characterized by few low-relief structures lacking faults (Figure 1b,c) [72]. After a nearly 130 Ma (Silurian and Devonian) absence of deposition, the basin began to accept deposition again in the late Carboniferous (Figure 1d). And the Early Permian Shanxi formation of the Daniudi Gas Field is dominated by braided river delta plain deposits, which developed in the marine continental transitional environment [73,74]. The Shanxi Formation varies in thickness from 25 to 87 m and consists of two sub-members, P_1s^1 and P_1s^2 (Figure 1e). The P_1s^1 is further divided into three sub-members and six sub-layers, including P_1s^{1-1-1} , P_1s^{1-1-2} , P_1s^{1-2-1} , P_1s^{1-2-2} , P_1s^{1-3-1} , and P_1s^{1-3-2} in ascending order; and P_1s^2 is divided into two sub-members and four sub-layers, including P_1s^{2-1-1} , P_1s^{2-1-2} , P_1s^{2-2-1} , and P_1s^{2-2-2} (Figure 1e). It mainly consists of grey medium-coarse sandstone, glutenite, and conglomerate. A black and dark grey carbonaceous mudstone interbed and coal seams were developed in P_1s^1 (Figure 1e) [72].

3. Samples and Methods

This work was conducted using cores and 56 thin sections from 21 wells drilled in the Shanxi Formation of the Daniudi Gas Field (Figure 1c). The thin sections were impregnated

with blue epoxy under a vacuum and stained with alizarin red-S and K-ferricyanide. Pure calcite is recognized by a pink stain, and ankerite by a blue stain.

The detailed core and thin section descriptions allowed us to identify the fine compositions of tight sandstone. The thin section descriptions were performed using an Optec BK-POL Digital Polarizing Microscope under transmitted light, using both plane-polarized and cross-polarized light. The percentages of the detrital compositions, matrix, and cements were determined through at least 300 points counts per thin section. A total of 18 samples were counted using an ELM-3R-Leica DMLP cathodoluminescence (CL) Microscope at the Craton Technology Co., Ltd., Beijing, China, for visual analyses. The resolution ratio and accuracy are estimated to be within 0.01 mm for CL imaging.

In order to characterize the morphologies and types of tuffaceous matrix, our study examined 11 samples. These samples were subjected to analysis using a JSM-7800F scanning electron microscope (SEM) equipped with energy-dispersive X-ray spectra (EDX). This analysis took place at the Chongqing Key Laboratory of Nano/Micro Composite Materials and Devices.

For the investigation of trace elements, a total of 9 samples were selected for analysis. These included 2 samples of tuffaceous mudstone, 2 samples of siltstone, 1 sample of silty mudstone, 1 sample of mudstone, 1 sample of coal, and 2 samples of tuff. The analysis of trace elements was conducted by Craton Technology Co., Ltd., Beijing, China. The rock powers were first digested by HF + HNO₃ in Teflon bombs and analyzed with a ThermoFisher ICAP-RQ ICP-MS. The detailed sample-digesting procedure for ICP-MS analyses by Zhang et al. (2012) was followed [75]. Two standard rocks, GSR2 and GSR5, were chosen for calibrating the element concentrations of the measured samples. The accuracy is estimated to be within 10% for trace elements.

4. Results

4.1. Petrological Characteristics

The results of the core and thin-section observations indicate that the lithology of the Shanxi Formation in the Daniudi Gas Field predominantly consists of sandstone, mudstone, and coal, with occasional occurrences of conglomerate and tuff (Figure 2).

In the study area, the primary type of sandstone is litharenite, followed by lithic graywacke (Figure 3). The sandstone grain size exhibits significant variation, with the primary particle size distribution ranging from 0.4 to 1.4 mm. Furthermore, the particle rounding degree varies from subangular to angular (Figure 2e–j). The detrital component of glutenite is primarily quartz and diverse lithic fragments (Table 1). The feldspar content is notably low, with most crystals having undergone kaolinization or replacement by calcite, ferroan calcite, or complete dissolution (Figure 2f). The lithic fragments include metamorphic, sedimentary and igneous rocks (Figure 2e,g–i). The fragments of metamorphic rocks are of slate, phyllite, metasandstone, schist, and mylonite. Other lithoclasts are of mudstone and sandstone, while igneous fragments are of granite, rhyolite, and tuff.

The matrix is terrigenous and tuffaceous (Table 1). The content of the tuffaceous matrix is relatively high and will be described in detail in the following sections. The cement is mainly composed of siliceous and calcareous material (Table 1; Figure 2j), followed by clay minerals such as kaolinite, illite, and chlorite.

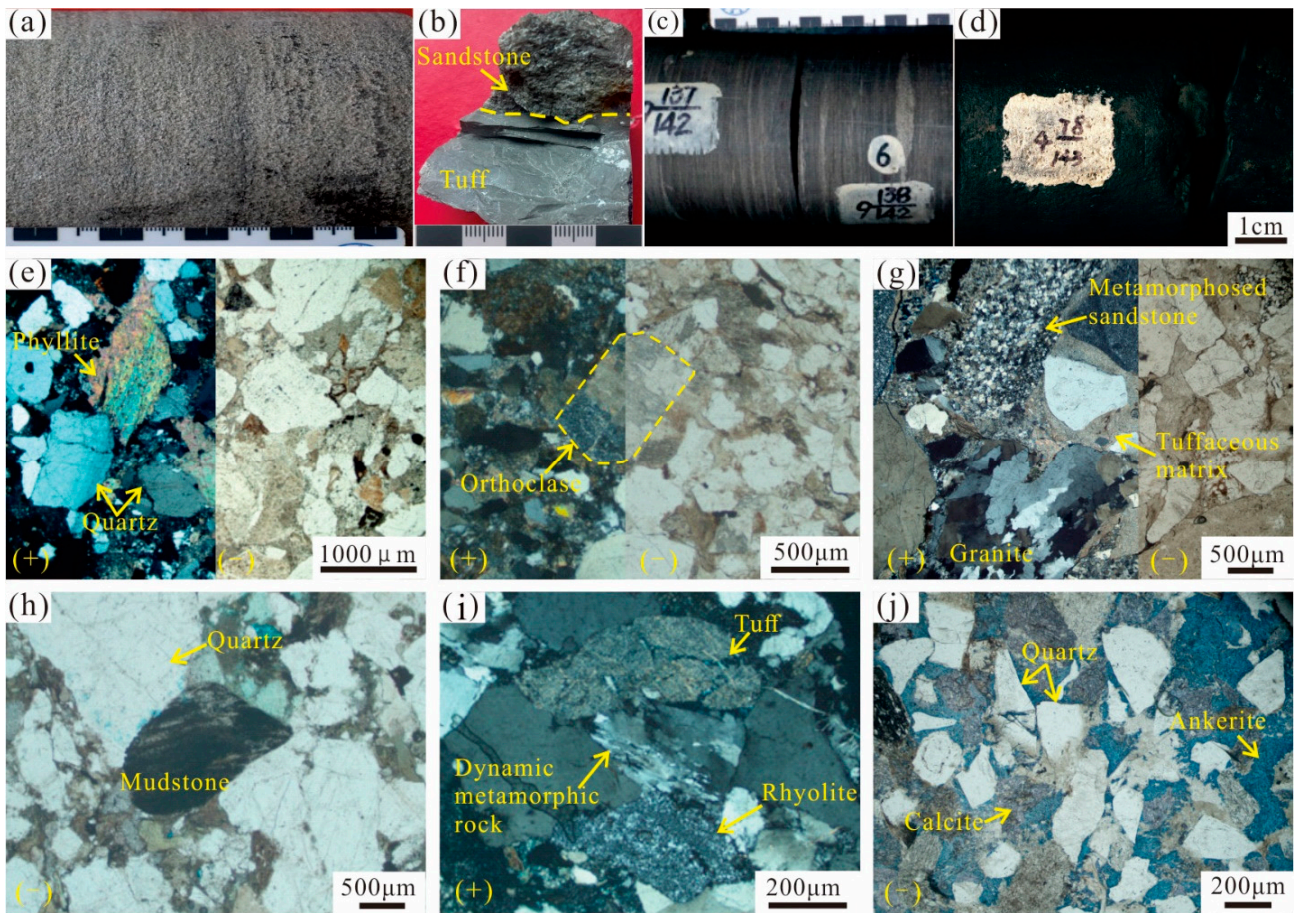


Figure 2. Petrological characteristics of the Shanxi Formation in the Daniudi Gas Field based on cores and thin sections. (a) Grey medium granular sandstone, parallel bedding, 13–2730.4 m. (b) The upper part is grey coarse granular sandstone, and the lower part is light grayish green tuff, 11–2699.0 m. (c) Dark grey mudstone with sandy banding, horizontal bedding, 10–2656.1 m. (d) Black coal, 42–2569.0 m. (e) Quartz and phyllite fragment, 44–2576.0 m. (f) Orthoclase metasomated by calcite; Carlsbad twin could be recognized; 39–2731.1 m. (g) Metamorphosed sandstone and granite fragment, tuffaceous matrix altered to sericite, 14–2812.5 m. (h) Quartz and mudstone fragment, 12–2789.1 m. (i) Dynamic metamorphic rock, rhyolite, tuff and granite fragment, sub-rounded quartz, 13–2706.0 m, (j) Calcite metasomatism, ankerite cementation, angular quartz, 11–2701.2 m.

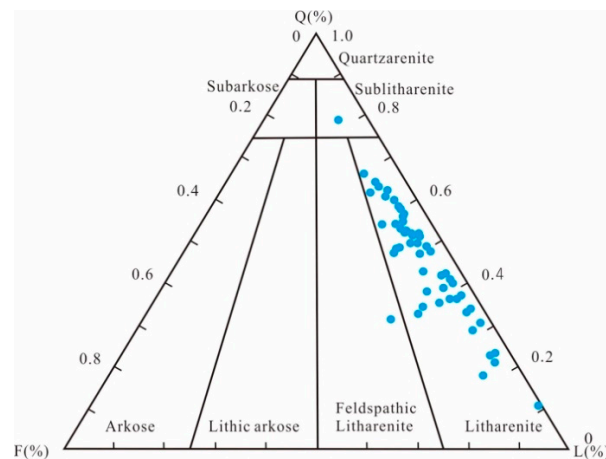


Figure 3. Sandstone composition of the Shanxi Formation in the Daniudi Gas Field refer to Folk, (1974) [76]. The blue dots are the data from this study.

Table 1. Percentages of detrital compositions, matrix, cements, and porosity for the Shanxi Formation in the Daniudi Gas Field (%).

Well	Depth (m)	Quartz	Feldspar	Mica	Other Minerals	Lithic Fragment						Matrix				Cement			Porosity (%)						
						Granite	Rhyolite	Basalt and Andesite	Tuff	Slate	Phyllite	Schist	Meta-Sandstone	Dynamic Metamorphic Rock	Mudstone	Sandstone	Tuffaceous	Terrigenous		Ankerite	Ferrous Calcite	Siliceous Cement	Calcite	Argillaceous Cement	
12	2777.5	38				18	15		5	1		3	2	0.5		8	2				0.5		1		6
12	2772.2	45	2	1		4	12		15	1			2			10	2				0.5		1.5		2
12	2745.8	45				15	10		10			1			1	5	2	1			1		1		8
12	2745.0	50		1	0.5	8	5		8		1		1	2		15	3				1		3		1.5
12	2747.6	40				19	15		4			1	2	1		8	1		1		2		2		4
13	2792.0	48	1	1	2	4	10		7	1			1	4		12	2	2.5			0.5		1		3
13	2779.2	50		1		3	20		3		1		1	6	1	6	4				0.5		1.5		2
13	2775.6	31				22	20		5	0.5		5	2	3		4	2.5						3		2
13	2748.1	30	1			8	29		5	2		4			10	4	1				0		2		4
13	2732.2	15	5			30	13	0.5	5			3		2		6	2				1	8	1.5		8
13	2729.4	35				15	10		3			4	1	1		12	2				2		2		13
11	2798.8	30	2			20	10		4			3	3			8	2				0.5	1.5	3		13
11	2776.4	50				10	12		1	1		2	0.5			8	1	4			1.5	0	1		8
11	2728.8	36	2	0.5		8	15	1.5	10			2	3	3		8	4				0.5		2		4.5
11	2701.2	25	12	1	1	10	7	1.5	5	1	3	1	1	3		6	1	20					1		0.5
14	2812.5	30	1			20	15		3				1	2		15	2	1			1		2		7
14	2792.1	40	1			11	13		3			2				8	1	3	2		2		2		12
14	2775.2	40	4	1		3	5		15	1			1	2	0.5	10	3	8			0.5		2		3
10	2683.5	59	1	0.5		5	8		3	1		1	0.5	1		10	1	0.5			1	0.5	2		5
10	2659.8	43				8	5.5		8		3	2	1	2		12	2	5			1		1		6.5
10	2645.6	40	5		0.5	6	13		5	1		3		2		7	3	3	1		3		2		5.5
10	2679.6	43				12	15		3			1	2		3	8	0.5	1			1		0.5		10
9	2591.3	27	8	3	2	8	12	1	10	1			2	2		10	3			5	0.5		3		1.5
9	2570.7	30	7	1		8	13		5	1	3		2	3	2	5	3	2	7		1		3		2
9	2569.3	21	1			15	25	1	12	1		2		1		5	2	2	0		1	1	2		8
87	2697.3	60				5	10		4	1	1		1.5	1		9	2	1			0.5		1		3
87	2684.5	25	1			21	10		5				4			10	2				3	2	2		15

Table 1. Cont.

Well	Depth (m)	Quartz	Feldspar	Mica	Other Minerals	Lithic Fragment						Matrix					Cement			Porosity (%)					
						Granite	Rhyolite	Basalt and Andesite	Tuff	Slate	Phyllite	Schist	Meta-Sandstone	Dynamic Metamorphic Rock	Mudstone	Sandstone	Tuffaceous	Terrigenous	Ankerite		Ferroan Calcite	Siliceous Cement	Calcite	Argillaceous Cement	
86	2626.5	54	1			5	7		2				4	1	3		2	2			3		2	4	
86	2585.1	50	0.5	0.5		5	8		8	1	2		4	1	2		15	2			1		2	2	
21	2665.6	35				20	15		2	1	2		5	2	1	1	10	1			0.5	0.5	1	4	
21	2646.4	30			2	25	12		1				1	2	2	4	10	1.5			2		1	6	
21	2602.6	35	5			15	9		8				4	2	2		3	3			1	5	2	6	
22	2656.4	40	5.5			10	10		4	1			4	2	2	1	6	2			3.5	8	1	6	
22	2654.9	40	2		1	12	5		5				3	2	1		13	2					1	13	
25	2676.8	40	2			8	10		3					1			10	1		10	2		1	12	
25	2596.9	65	2			1	7		8					1	1		4	2			3	1	2	3	
24	2751.9	18	2			18	26		3				6	2			5	1		1	12	1	0	1	4
24	2708.3	50	2			6	10		6	1	1		2	2			10	3			1		3	3	
31	2808.5	55		1		8	5.5		5					5	2	1	7	2			0.5		1	7	
31	2802.6	40		1		10	14		5	1				1			10	2			1.5	0.5	2	12	
108	2615.2	55	1			12	4		2	1			1	1			6	3		0.5	0.5		1	12	
108	2548.3	45	2			5	12		6	0.5				1		2	12	2			0.5		2	10	
18	2744.5	40				10	2		4	1	1						4	1.5		3	25	0	6	2	0.5
18	2696.1	45			1	5	10		8				4	2			10	6				2.5		3	1.5
18	2663.3	37	1			8	10		8				1		9		13	3.5			0.5		3	4	
28	2619.7	25	2			15	22		3	2			4	3			10	3		2		1	2	1	5
28	2587.8	10				28	35		3.5		0.5		4	2			5	2			3		1	6	
28	2562.9	30	4	1		13	15		8	2			4	2			8	3			5.5	0.5	3	5	
94	2683.3	20	2			10	25		10	1			3	3		2	15	1			2.5		1.5	3	
94	2669.1	35	3			19	8		3				2				8	2			5	2	1	11	
40	2692.3	45	1			12	8		3				1	1	5		5	2			1		2	14	
40	2679.1	50	2	3		3	12		10		2		1	1	2		6	2			1		2	3	
1-4-1	2879.5	69				4	2										6	1.5			4		1	12	

4.2. Volcanogenic Components

4.2.1. Quartz

The quartz content ranges from 10% to 69% (average 39.3%) (Table 1). The quartz is mainly derived from metamorphic rocks, sedimentary rocks, and igneous rocks; authigenic quartz formed during diagenesis could also be identified. The high-temperature magmatogenic quartz shows a blue-purple color in the CL image (Figure 4a), which can be used to distinguish it from other types of quartz. However, it is still hard to distinguish the volcanogenic quartz and intrusive quartz from each particle. Still, some discriminant marks could be used to recognize the typical volcanogenic quartz, such as irregular shapes, angular shapes, partly embayed boundaries, or inward arc boundaries caused by high-temperature erosion, as well as rare abrasion marks caused by transportation (Figure 4b). The analysis of thin sections and CL images shows that the average volcanogenic quartz content is about 5%.

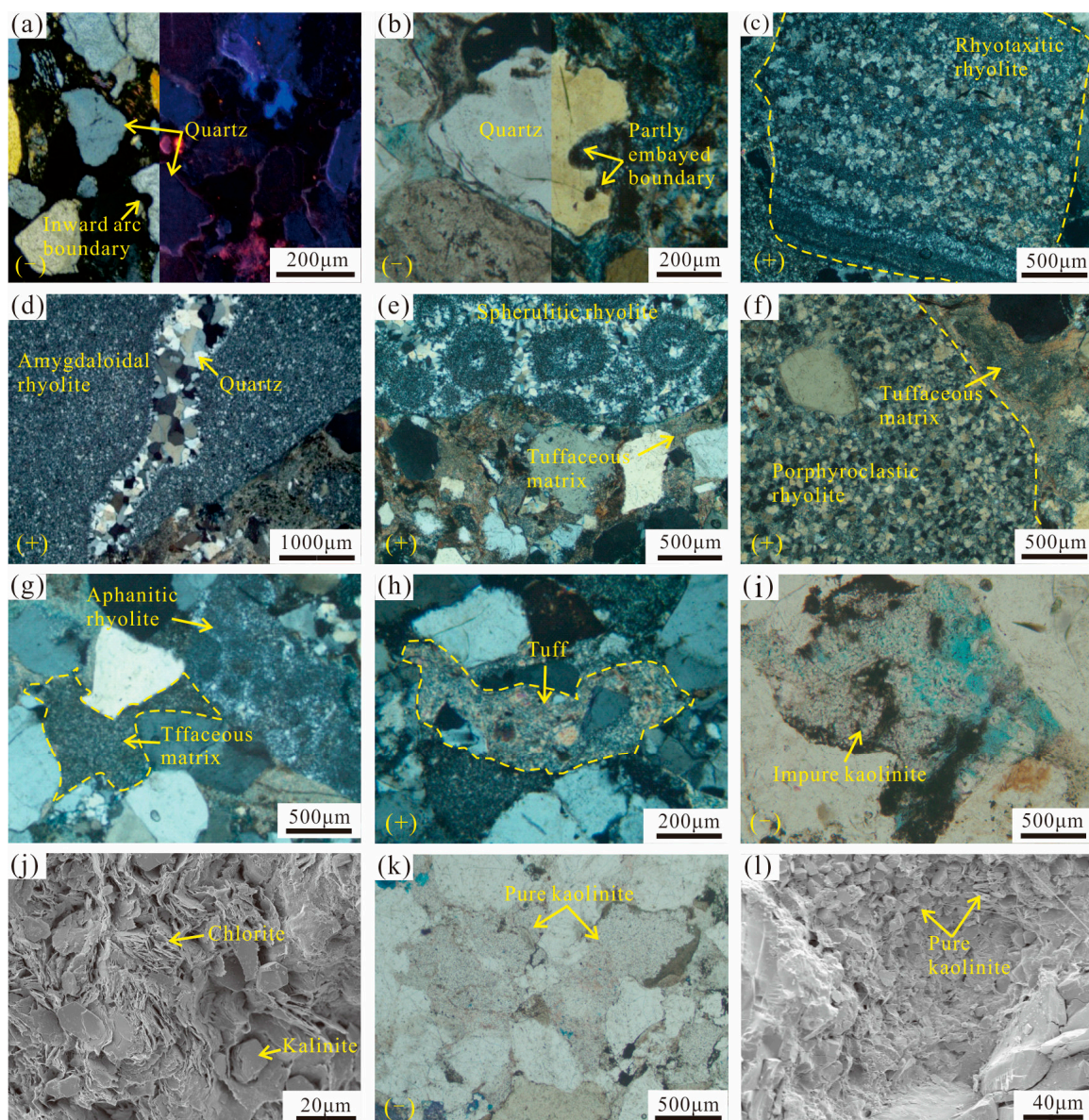


Figure 4. Photomicrographs of volcanogenic components in the Shanxi Formation. (a) Quartz with inward arc boundary, which shows as blue-purple in the CL image (right), 11–2725.9 m. (b) Quartz with partly embayed boundary, 24–2703.3 m. (c) Rhyolitic structure rhyolite fragment, 12–2787.8 m.

(d) Amygdaloidal rhyolite fragment; elongated vesicle fully filled with multi-stage quartz, 14–2812.5 m. (e) Spherulitic rhyolite fragment; tuffaceous matrix shows “pores fully filled”, 12–2779.5 m. (f) Porphyroclastic rhyolite fragment; tuffaceous matrix altered to sericite, 14–2812.5 m. (g) Aphanitic rhyolite fragment; tuffaceous matrix shows “fully filled pores” and converted to crystalline felsic minerals, 12–2787.8 m. (h) Tuff fragment with angular quartz crystal, 39–2734.3 m. (i) Impure kaolinite, 13–2729.4 m. (j) Impure kaolinite, the mixture of kaolinite and chlorite in the SEM image, 13–2729.4 m. (k) Pure kaolinite, 18–2686.0 m. (l) Pure kaolinite in the SEM image, 18–2686.0 m.

4.2.2. Lava Fragments

The major lava fragments are rhyolite fragments and sporadic basalt. Andesite fragments could be found in a few thin sections. The lava fragment content varies from 2% to 29%, with an average of 11.5%. The rhyolite fragments display a complex texture and structure, allowing for the identification of various types. (1) Rhyotaxitic rhyolite shows typical rhyotaxitic texture and lacks phenocrysts (Figure 4c). (2) Amygdaloidal rhyolite is characterized by a lower degree of crystallinity and elongated vesicles filled with multi-stage quartz (Figure 4d). (3) Spherulitic rhyolite displays spherulitic textures of various shapes and sizes (0.1 to 0.6 mm) (Figure 4e). These spherulites come in two main types: one with a central nucleus surrounded by cyclic minerals and annular aphanitic felsic minerals, and the other with minimal or no central nucleus and radial felsic minerals around it. (4) Porphyroclastic rhyolite features a porphyritic texture with varying degrees of matrix crystallization, ranging from aphanitic to fine-grained (Figure 4f). The phenocryst content is less than 3%, with most of the phenocrysts being quartz, and occasional feldspar phenocrysts that have fully dissolved. (5) Aphanitic, microcrystalline rhyolite, is characterized by poorly crystallized felsic minerals without a typical rhyolitic structure, vesicles, spherulitic textures, or phenocrysts (Figure 4g). These may represent fragments of other rhyolites.

The basalt and andesite fragments are in marked contrast to the felsic fragments under the plane-polarized light due to their darker appearance. Quartz crystallized from magma is too hard to identify. In cross-polarized light, the basalt matrix is characterized by an intersertal texture. Mafic minerals within the basalt have undergone alteration, resulting in the presence of chlorite, sericite, and other minerals. The andesite fragments exhibit a porphyroclastic texture, in which the feldspar phenocrysts have been totally replaced by quartz, and the interpenetration texture in matrix can still be recognized.

4.2.3. Tuff Fragments

The tuff fragments, ranging from 1.0% to 15.0% (average 5.4%), are mainly composed of volcanic ash, which has altered to sericite, kaolinite, and chlorite, or has been converted to felsic minerals through devitrification (Figure 4h). A few angular quartz crystals could be found in some tuff fragments (Figure 4h). The tuff fragments are characterized by semi-plastic deformation during strong compaction. Rigid particles, such as quartz and granite fragments, etc., are squeezed into the semi-plastic tuff fragments and are common in the tight sandstone of the Shanxi Formation (Figure 4h). Although they were easy to deform during strong compaction, the previous particle boundary of the tuff fragment can be identified (Figure 4h), indicating that the intergranular pores would not be fully filled by the deformed tuff fragments, which are obviously distinct from the tuffaceous matrix.

4.2.4. Tuffaceous Matrix

The tuffaceous matrix is derived from unconsolidated volcanic ash probably transported from its origin via the river or air. Its content ranges from 3.0% to 15.0% (with an average of 8.2%). The tuffaceous matrix exhibits plastic deformation during intense compaction, and intergranular pores are often filled by irregularly shaped tuffaceous matrix (Figure 4f,g,i–l), called “pores fully filled” [77,78], which is similar to the deformation of soft sediments. Pores fully filled indicates that the tuffaceous matrix has never been compacted before being deposited with other clastic particles.

The tuffaceous matrix is colorless or light brown in plane-polarized light and can be divided into four types based on cross-polarized light and SEM analysis. Furthermore, the dissolution simulation experiment conducted by Wang et al. (2005) [77] and the burial history of the Upper Paleozoic in the Daniudi Gas Field, as completed by Yang et al. (2010) [1], could help us better understand the genesis of the four types of tuffaceous matrix. (1) Sericite, micro-scaly with a bright II~III order interference color (Figure 4f), was formed in a closed diagenetic environment. In such conditions, the tuffaceous matrix remains relatively unaffected by dissolution, while its thermal evolution intensifies with increasing burial depth. The homogenization temperature of fluid inclusions ranges from 160 °C to 170 °C in some authigenic quartz in the Upper Paleozoic of the Daniudi Gas Field [1]. The temperature is very close to very low-grade metamorphism, and the tuffaceous matrix is converted to sericite through metamorphic recrystallization. (2) Fine felsic minerals: in a closed condition, the unstable amorphous volcanic ash will convert to crystalline felsic minerals, which shows weak optical characteristics without optical orientation in cross polarized light (Figure 4g). (3) Impure kaolinite formed in an open diagenetic environment, and the tuffaceous matrix underwent intense dissolution. The differentiation of various elements such as Si, Al, K, Na, and Ca depends on cationic reactivity. As a result, the tuffaceous matrix evolves into a mixture of kaolinite and chlorite in SEM images, referred to as impure kaolinite in plane-polarized light (Figure 4i,j). (4) Pure kaolinite, which formed in a more open diagenetic environment, experiences the transport of Si and Al by diagenetic fluids to adjacent pores. Consequently, pure kaolinite is deposited (Figure 4k,l), and only a few instances of chlorite mixed with kaolinite were observed in pure kaolinite (Figure 4k,l).

4.2.5. Volcanic Ash Layers

At least two volcanic ash layers were discovered in the Shanxi Formation during core observation. These ash layers are embedded within sandstone with a range from 4 to 6 cm. They are light green-gray and feel exquisite and smooth (Figure 2b). Notably, these layers stand in stark contrast to the adjacent dark-colored mudstone interlayers, which appear predominantly black or dark grey. Additionally, there is an absence of observable sedimentary transport characteristics at the base of these volcanic ash layers. The thin section observation shows that the volcanic ash has been converted to sericite and various clay minerals.

4.3. Trace Elements

The immobile trace elements in terrigenous clastic rocks, such as La, Th, Zr, Sc, Co, etc., are characterized by relative high stability, which could be used to constrain the provenance and tectonic setting [79,80]. The results of trace element analysis are given in Table 2, and the Post-Archaean Average Shale (PAAS)-normalized trace element spidergram [81] is shown in Figure 5.

The concentrations of the trace elements in the investigated fine-grained sedimentary rocks vary significantly. The content of high field strength elements (Zr, Hf, Y, Th, Nb, and Ta) and transition trace elements (V, Cr, Co, and Ni) ranges from 13 to 2707.4, 11 to 2784.0, and 87 to 2699.6, respectively, which is generally lower than that of PAAS. However, the concentrations in the remaining samples are higher than those in PAAS (Table 2; Figure 5). The content of Sc and La in most samples is higher than that of PAAS. In contrast, the content of large ion lithophile elements (LILE, Rb, Sr, Cs, and Ba) is lower than that of PAAS (Table 2; Figure 5).

Table 2. Trace elements contents for the Shanxi Formation fine-grained sedimentary rocks and tuff ($\mu\text{g/g}$).

Samples	13-2707.4	14-2813.1	11-2781.0	11-2784.0	87-2699.6	24-2760.3	87-2697.7	11-2699.0	24-2753.6
Lithology	Tuffaceous Mudstone	Tuffaceous Mudstone	Siltstone	Siltstone	Mudstone	Silty Mudstone	Coal	Tuff	Tuff
Li	22.94	157.84	7.46	35.99	56.01	154.48	206.95	29.59	17.59
Be	1.68	7.71	4.94	1.97	2.55	4.28	5.27	3.65	11.78
Sc	16.99	23.56	29.84	17.14	18.44	10.92	19.94	31.95	4.31
V	88.09	52.82	424.61	106.13	130.56	25.07	96.80	238.80	12.79
Cr	54.91	29.33	171.34	79.12	107.72	13.00	37.89	135.74	7.40
Co	11.64	3.09	98.94	23.69	19.43	4.12	4.09	32.03	25.66
Ni	13.69	8.82	29.70	22.38	31.25	7.80	22.01	35.18	18.18
Cu	29.90	17.67	11.79	28.86	36.98	8.26	13.27	8.43	10.83
Zn	426.84	17.79	26.63	132.55	108.81	13.36	17.70	98.53	9.48
Ga	14.38	45.76	45.66	23.73	27.09	24.84	44.88	53.01	27.34
Rb	63.57	14.96	272.92	102.10	139.91	9.40	51.99	184.70	1.58
Sr	71.28	77.42	299.29	103.47	117.42	204.48	79.18	298.25	48.52
Y	35.34	77.14	40.43	34.77	30.90	38.94	35.43	45.02	28.16
Zr	81.13	1970.04	268.05	147.08	139.58	404.01	656.74	396.11	114.13
Nb	9.87	170.95	28.14	15.44	18.63	42.99	39.07	56.18	9.43
Mo	0.18	1.92	0.16	0.42	0.44	1.27	0.70	0.27	3.68
Cd	1.55	0.00	0.03	0.35	0.26	0.03	0.01	0.03	0.04
In	0.16	0.32	0.12	0.11	0.11	0.15	0.22	0.11	0.06
Sb	0.12	0.65	1.12	0.32	0.25	0.24	0.11	0.25	0.35
Cs	3.42	0.94	10.18	5.74	8.68	0.48	6.48	7.38	0.09
Ba	308.30	316.38	814.12	361.45	611.65	92.72	427.08	537.82	41.85
Hf	2.11	55.57	7.98	3.85	3.56	12.91	17.87	11.03	3.09
Ta	0.71	16.21	2.10	1.11	1.19	3.16	2.60	3.02	0.59
Tl	0.38	0.11	1.91	0.67	0.79	0.11	0.50	0.94	1.91
Pb	20.61	125.35	56.11	29.83	34.95	29.16	27.45	46.11	56.11
Bi	0.22	1.31	0.88	0.34	0.38	0.82	0.84	0.22	0.88
Th	1.95	8.53	9.95	2.97	3.16	6.50	6.90	8.83	9.95
U	8.46	84.56	29.70	14.49	15.62	17.69	33.09	39.11	29.70

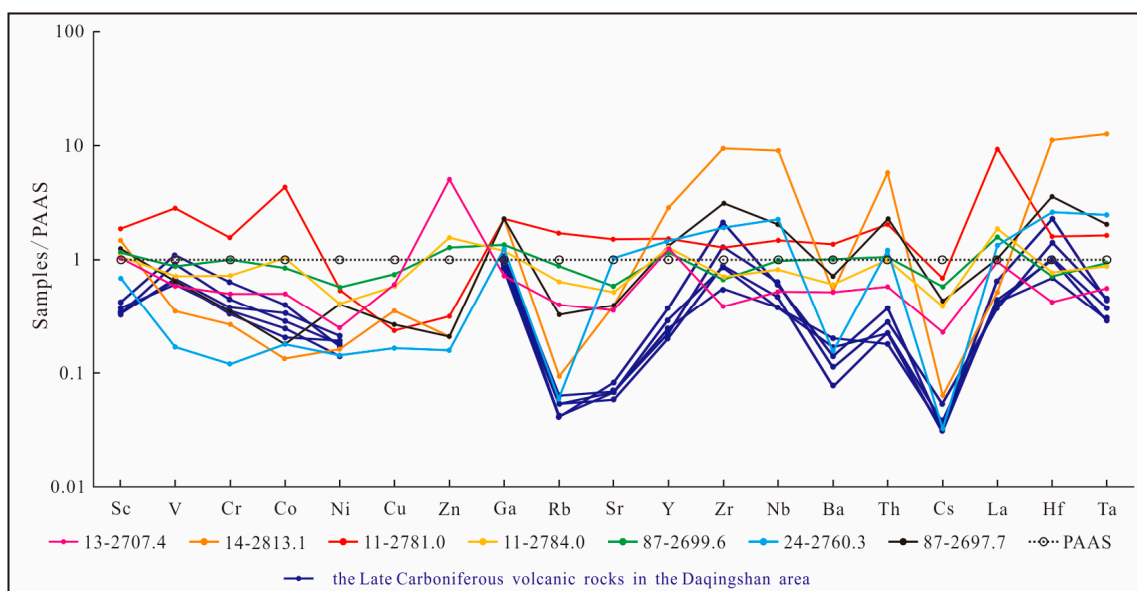


Figure 5. Trace elements spidergram of the investigated fine-grained sedimentary rocks normalized to PAAS following Taylor and McLennan, (1985) [81], and the data of the Late Carboniferous volcanic rocks in the Daqingshan area refers to Zhang et al., (2018) [82].

4.4. Rare Earth Elements

The results of rare earth element (REE) analysis are given in Table 3. To better understand the possible provenances, the Chondrite-normalized REE patterns [81] are shown in

Figure 6. The total REE content in terrigenous clastic rocks (Σ REE) varies from 167.20 $\mu\text{g/g}$ to 1134.65 $\mu\text{g/g}$, with an average of 369.28 $\mu\text{g/g}$ (Table 3). Σ REE is higher than that of the Upper Crust (UC, 146.37 $\mu\text{g/g}$) and the Post-Archaean Australian Shales (PAAS, 183.00 $\mu\text{g/g}$) [64]. Additionally, the ratio of (Σ LREE/ Σ HREE) ranges from 2.38 to 28.48 (average 11.36) (Table 3), which is also higher than that of UC (9.54 $\mu\text{g/g}$) and PAAS (9.52 $\mu\text{g/g}$). Furthermore, the Eu anomaly (Eu/Eu*) varies between 0.44 and 0.69 (average 0.57) (Table 3). The distribution curves of LREE are relatively steep, while the curves of HREE are relatively flat (Figure 6). These curves show an obvious “V” shape at Eu, indicating negative Eu anomalies (Figure 6 orange line).

Table 3. Rare earth element contents for the Shanxi Formation fine-grained sedimentary rocks and tuff ($\mu\text{g/g}$).

Samples	13-2707.4	14-2813.1	11-2781.0	11-2784.0	87-2699.6	24-2760.3	87-2697.7	11-2699.0	24-2753.6
Lithology	Tuffaceous Mudstone	Tuffaceous Mudstone	Siltstone	Siltstone	Mudstone	Silty Mudstone	Coal	Tuff	Tuff
La	36.63	19.68	362.04	71.75	60.37	51.06	38.85	242.76	59.24
Ce	77.01	51.55	540.65	156.64	121.20	137.51	72.64	460.75	122.45
Pr	8.36	6.86	49.06	20.08	13.81	15.12	7.10	49.28	16.19
Nd	30.24	31.37	128.47	80.14	47.95	42.34	21.63	155.53	61.44
Sm	5.93	12.50	13.48	14.81	8.56	5.85	5.49	20.46	12.22
Eu	1.25	1.64	2.45	1.97	1.73	0.91	1.21	2.93	1.48
Gd	5.24	10.34	14.40	9.52	7.08	5.60	5.70	14.12	8.80
Tb	1.00	2.82	1.44	1.58	1.27	1.14	1.19	1.67	1.47
Dy	5.29	16.15	6.60	8.21	5.74	6.84	6.08	7.57	6.63
Ho	1.03	3.04	1.44	1.26	1.05	1.41	1.05	1.73	1.14
Er	3.12	8.20	5.38	3.40	2.78	4.33	2.75	5.93	3.05
Tm	0.49	1.34	1.00	0.54	0.48	0.74	0.44	1.06	0.46
Yb	3.11	8.98	7.20	3.87	3.09	5.02	2.70	7.52	2.84
Lu	0.49	1.14	1.03	0.48	0.43	0.67	0.39	1.16	1.03
La _N /Yb _N	11.79	2.19	50.26	18.52	19.54	10.18	14.38	32.29	50.26
Σ REE	179.18	175.62	1134.65	374.25	275.53	278.51	167.2	972.48	297.84
Σ HREE	19.76	52.01	38.5	28.87	21.92	25.74	20.29	40.76	24.81
Σ LREE	159.42	123.61	1096.16	345.38	253.61	252.77	146.92	931.72	273.03
Σ LREE/ Σ HREE	8.07	2.38	28.48	11.96	11.57	9.82	7.24	22.86	11.00
Eu/Eu*	0.69	0.44	0.54	0.51	0.68	0.48	0.66	0.53	0.44
Gd _N /Yb _N	1.37	0.93	1.62	1.99	1.86	0.90	1.71	1.52	2.51

La_N/Yb_N, Eu/Eu* normalized by Chondrite and PAAS following Taylor and McLennan, (1985) [81]; δEu (Eu/Eu*) = (2Eu_N)/(Sm_N + Gd_N).

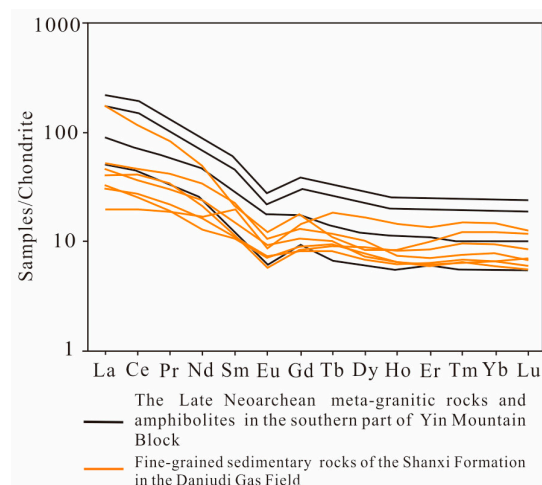


Figure 6. Chondrite-normalized REE patterns of the investigated fine-grained sedimentary rocks refer to Taylor and McLennan, (1985) [81], and the data of amphibolites in the southern part of Yin Mountain Block from Duan, (2021) [83].

5. Discussion

5.1. Contradiction between the Main Provenance of Shanxi Formation and Those Volcanogenic Components

Previous research has shown that the provenance of the Shanxi Formation in the Daniudi Gas Field was attributed to an active recycled-orogenic provenance and derived from metamorphic rocks of Precambrian succession in the ancient land of the Yin Mountain in the north of the Ordos Basin [9,10,12,13,26]. Our own data further corroborate these conclusions. The Dickinson triplots show a recycled-orogenic provenance (Figure 7a,b). The Rb and Ba content in the majority of terrigenous clastic rocks demonstrates depletion relative to PAAS (Table 2; Figure 5). It appears that Rb and Ba were flushed out from seawater by the incoming freshwater. As suggested by Norry et al. (1994) [84], these sediments might have undergone multiple cycles of weathering, erosion, and redeposition, potentially resulting in material being added or removed. The Chemical Index of Alteration (CIA, ranging from 83.96 to 99.06, averaged 91.65) results also indicate a strong weathering in the provenance. The Chondrite-normalized REE patterns are consistent with those of the Upper Crust (UC) and also align with those of Late Neoproterozoic (metamorphic) intrusive rocks such as amphibolite, plagioclase amphibolite schists, and tonalite, which are located in the southern part of the Yin Mountain Block (Figure 6). The strong and varied concentrations of the trace elements among different samples imply that the provenance and tectonic setting are complex. The volcanic arc orogenic belt is one of them (Table 3; Figure 5), which is also supported by the Th-Sc-Zr/10 and La-Th-Sc plots (Figure 8). The complex and mixed provenance and tectonic setting of the Shanxi Formation include an active continental margin with subductional orogeny and a trench–arc–basin system.

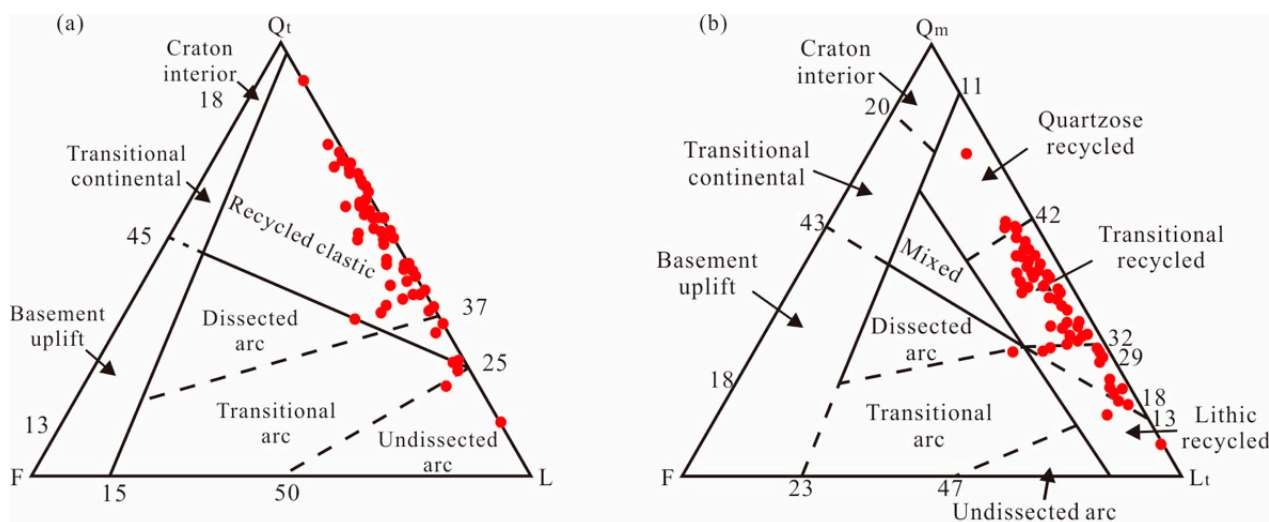


Figure 7. Provenance discrimination of the Shanxi Formation sandstones of the Daniudi Gas Field using the Qt-F-L (a) and Qm-F-Lt (b) diagram refer to Dickinson and Suczek, 1979 [85]. The red dots are the data from this study. Qt-Total quartzose grains, $Qt = Qm + Qp$; Qm-Monocrystalline quartz; Qp-Polycrystalline quartz; F-Total feldspar grains; L-Total unstable lithic fragments; Lt = L + Qp.

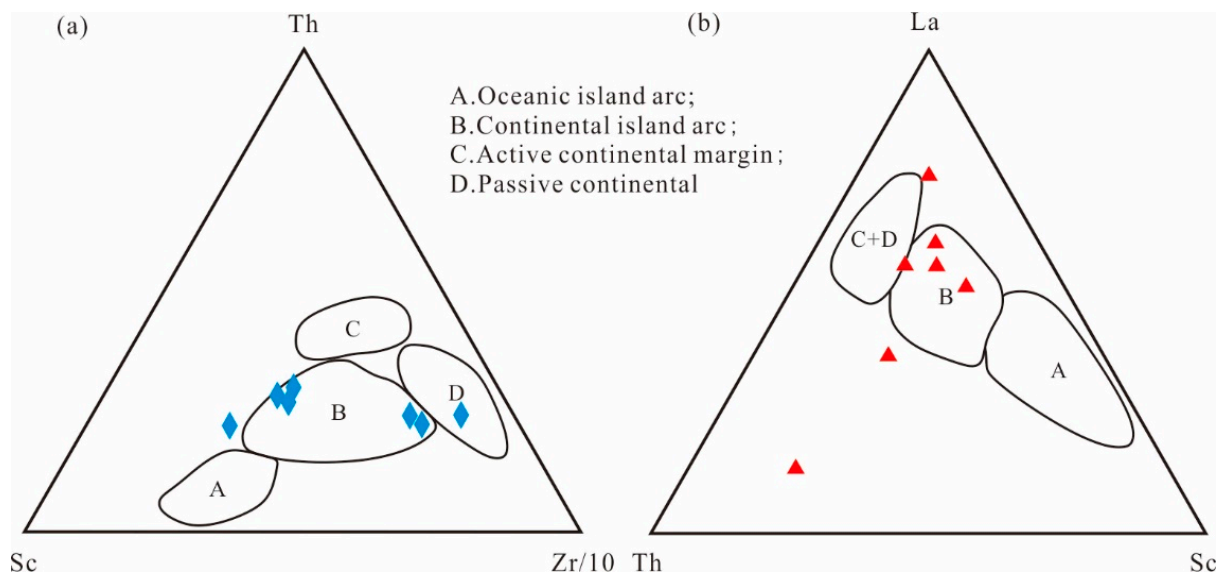


Figure 8. Discrimination diagrams of Th-Sc-Zr/10 (a) and La-Th-Sc (b) for the investigated fine-grained sedimentary rocks (Bhatia and Crook, 1986 [80]). Blue diamonds and red triangles are data from this study.

However, the cause of the high content of unmetamorphosed volcanogenic components discovered in the Shanxi Formation in the Daniudi Gas Field is still not well explained by previous research. The Precambrian succession in the ancient land of the Yin Mountain includes the Jining Group (Ar₁₋₂), Wulashan Group (Ar₃), Alashan Group (Ar₃-Pt₁), Sertengshan Group (Pt₁), Erdaowa Group (Pt₁²), and Chaertaishan Group (Pt₂), in ascending order. Only minor and metamorphic volcanic rocks developed in the Alashan Group and Chaertaishan Group [11,86]. It is impossible for the fresh and unmetamorphosed volcanogenic components in the Shanxi Formation to have derived from the Precambrian basement, especially the easily metamorphosed tuffaceous matrix and tuff fragments. There must be a younger provenance consistent with the depositional period of the Shanxi Formation, excluding the ancient basement. This implies that the volcanogenic quartz, lava fragments, tuff fragments, tuffaceous matrix, and volcanic ash layers must derive from volcanic eruptions that occurred earlier than or were coeval with the Shanxi Formation.

To better understand the relationship between the depositional age of the Shanxi Formation and the syn-depositional volcanism, we collected published age data of detrital zircons of the Shanxi Formation (Table 4). All results reveal a consistent age group at ca. 300 Ma except the Well Shuang157. But one grain still yielded the ²⁰⁶Pb/²³⁸U age of 295 ± 5 Ma in the Well Shuang157. Furthermore, the Carboniferous to Permian stratigraphy and timescale of the North China Plate have been systematically reconstructed by Shen et al. (2022) [24]. We therefore constrained the age of the Shanxi Formation at 298.18 ± 0.32 Ma to 295.65 ± 0.08 Ma in the north of the basin, and 295.346 ± 0.080 Ma to 293.0 ± 2.5 Ma in the south. The ages of detrital zircons obtained by Qu et al., 2020 [13], and Chen, 2020 [87], are more representative for our following discussion (Table 4). One of the age peaks of detrital zircon is 301 Ma dated by Qu et al. (2020) [13] and another peak is 304 Ma dated by Chen (2020) [87]. These zircon U-Pb ages are consistent with the depositional period of the Shanxi Formation in the north of the basin (295.3–298.2 Ma) [24]. Moreover, a previous study shows that the content of Gd in old strata is relatively higher than in young strata for the fractionation of Gd, and the (Gd/Yb)_N ratio could be used as a proxy for estimating the relative age of provenance [88]. In this regard, (Gd/Yb)_N values in terrigenous clastic rocks fluctuate from 0.90 to 1.99, with an average of 1.48 (Table 3), while the value of the Taiyuan Formation exceeds 2.00 [12]. The (Gd/Yb)_N ratio indicates a decrease in the contribution from the old provenance (the ancient basement) and an increase from the younger provenance from the Taiyuan Formation to the Shanxi Formation.

Table 4. Ages of sandstone detrital zircons of the Shanxi Formation in the Ordos Basin (LA-ICP-MS analyzed).

Section/Well of Sample	Formation	(Prominent Age Populations)/Major Age (Ma)			Reference	
North	Liuyin, Shanxi	Shanxi Fm.	(281~517)/ 301	(1711~2514)/ 1883	/	Qu et al., 2020 [13]
	Well Shen 68	Shanxi Fm.	(289~356)/ 304	(2491~1717)/ 1842, 2423	/	Chen, 2020 [87]
	Well Shuang 157	Shanxi Fm.	(2420~1701)/ 1873, 2440	/	/	Chen, 2020 [87]
	Xishan, Beijing	the middle of Shanxi Fm.	(262~368)	(2435~2291)	/	Yang et al., 2006 [89]
South	Yangcheng, Shanxin	the bottom of Shanxi Fm.	299	1 836	/	Zhu et al., 2014 [90]
	Well Qingtan 1	the 1st member of Shanxi Fm.	(287~339)/ 337	(385~466)/ 432	/	Luo et al., 2017 [91]
	Pingliang, Ganshu	Shanxi Fm.	(282~344)/ 286	(1717~2100)/ 1945	(2188~2497)/ 2355	Sun et al., 2020 [92]
	Well Qingtan 1, Well Su51, Well Chengtan 2, Erdaogou, Pingliang, Ganshu,	Shanxi Fm.	(300~450)/ ca. 300	(1824~1873)	(2440~2569)	Hu et al., 2023 [93]
	Tongchuan, Shanxi	Shanxi Fm.	364 946	450 2446	794 /	Wang et al., 2023 [94]

5.2. Provenance and Transportation of the Volcanogenic Components in the Shanxi Formation

5.2.1. Tectonic Framework and Sediment Routing System

In the latest Early Carboniferous to Early Permian, the northern margin of the North China Plate developed an Andean-style active continental margin which formed a volcanic arc and back-arc basin due to the southward subduction of the Paleo-Asian Ocean (Figure 9). At the same time, the northern part of the North China Plate began to uplift (Figure 10). That resulted in volcanic materials associated with continental arc widely appearing in the Inner Mongolia Paleo-uplift. The northern uplift started to supply materials to the northern part of the Ordos Basin. Those products of volcanic eruptions accumulated in the Inner Mongolia Orogenic Belt and formed the volcanic rock associations of Baolige Temple (C₂), Tsagaannuur (C₂), Dashizhai (P₁), and Elitu (P₁), with a thickness ranging from 1900 to 2400 m (Figure 9) [95]. In the Late Permian, the Inner Mongolia Paleo-uplift evolved to become the Xing-Meng Orogenic Belt due to the continent–continent collision between the North China Plate and the Siberia Plate. With continuous subduction and compression, the Yin Mountain (Yinshan Orogenic Belt or Yin Mountain uplift) uplifted at the southern part of the orogenic belt, and the thrust fault-fold developed at the north boundary of the North China Plate (Figures 9 and 10). Subduction-related magmatic activities also occurred in the Yin Mountain, which was proved by the intermediate-acid volcanogenic materials accumulation in the Daqingshan coal basin [96,97].

Previous studies have shown that Yinshan is the main provenance of the basin, and most areas of Yimeng Uplift and Hetao also rise southward with the uplift, becoming another provenance of the basin (Figures 9 and 10). The sedimentary system of the Shanxi Formation in the Ordos Basin transitioned an epicontinental sea deposit to a deltaic sedimentary system from the Taiyuan formation to Shanxi formation of the Early Permian [98,99]. The paleogeography and paleogeomorphology of P₁s¹ to P₁s² keep consistent during that period [99]. The basin gradually evolved into a continental environment due to marine regression [100]. During the deposition period of the Shanxi Formation, the paleogeomorphology of the basin was higher in the north and lower in the south, along with a central depression. The sediment system shows a nearly north–south trend. The sedimentary facies from north to south are alluvial plain, delta plain, delta front, and lake (Figures 9 and 10).

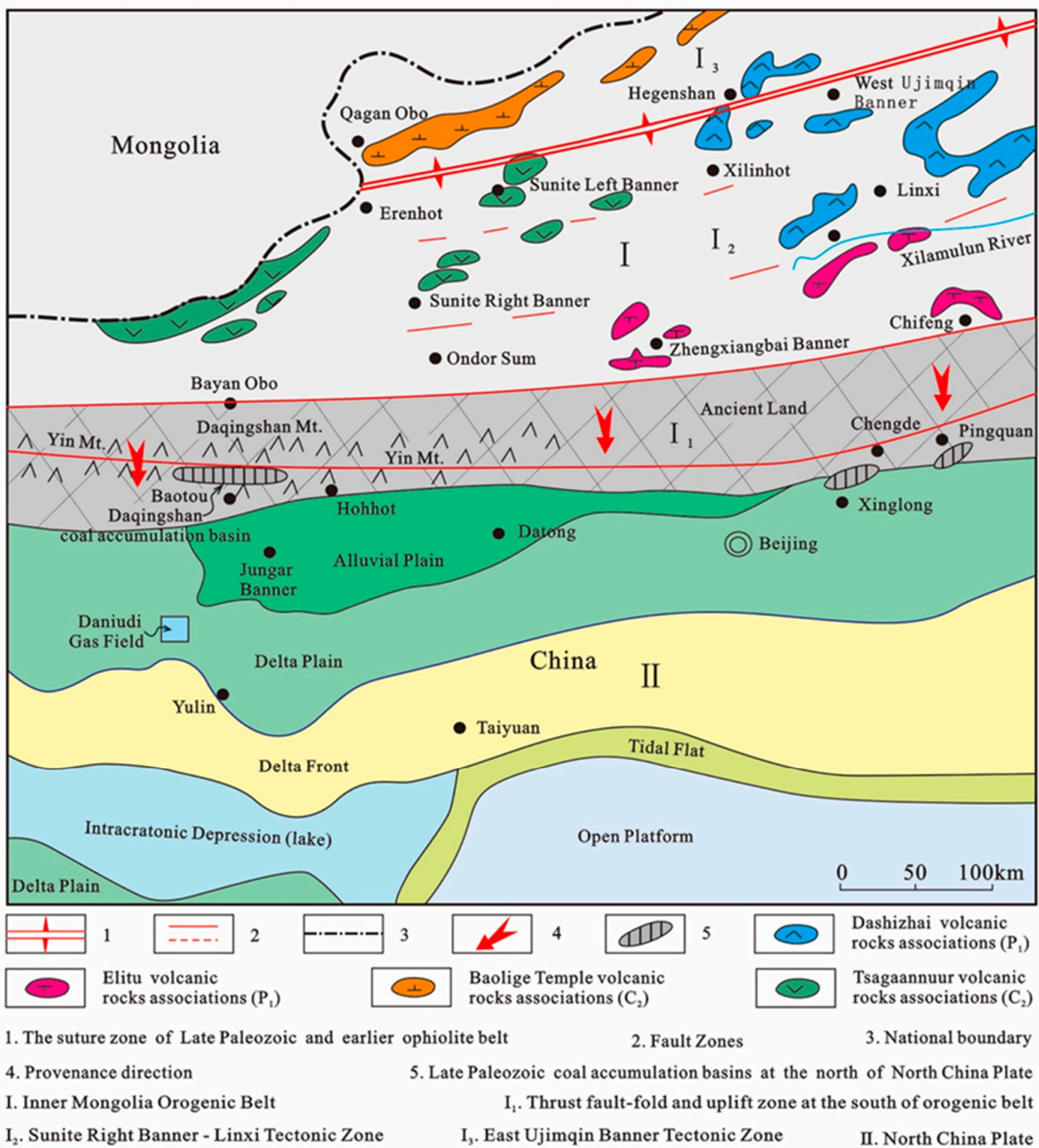


Figure 9. The tectonic framework and volcanic rocks distribution of the Inner Mongolia Orogenic Belt in the Late Paleozoic (modified after Zhou, 2000 [28] and Bureau of Geology and Mineral Resources of Inner Mongolia Autonomous Region, 1991 [95]) and the paleogeographic map of the 1st member of the Shanxi Formation of the northern part of the North China Plate (modified after Li et al., 2020 [98] and Zhai et al., 2023 [99]).

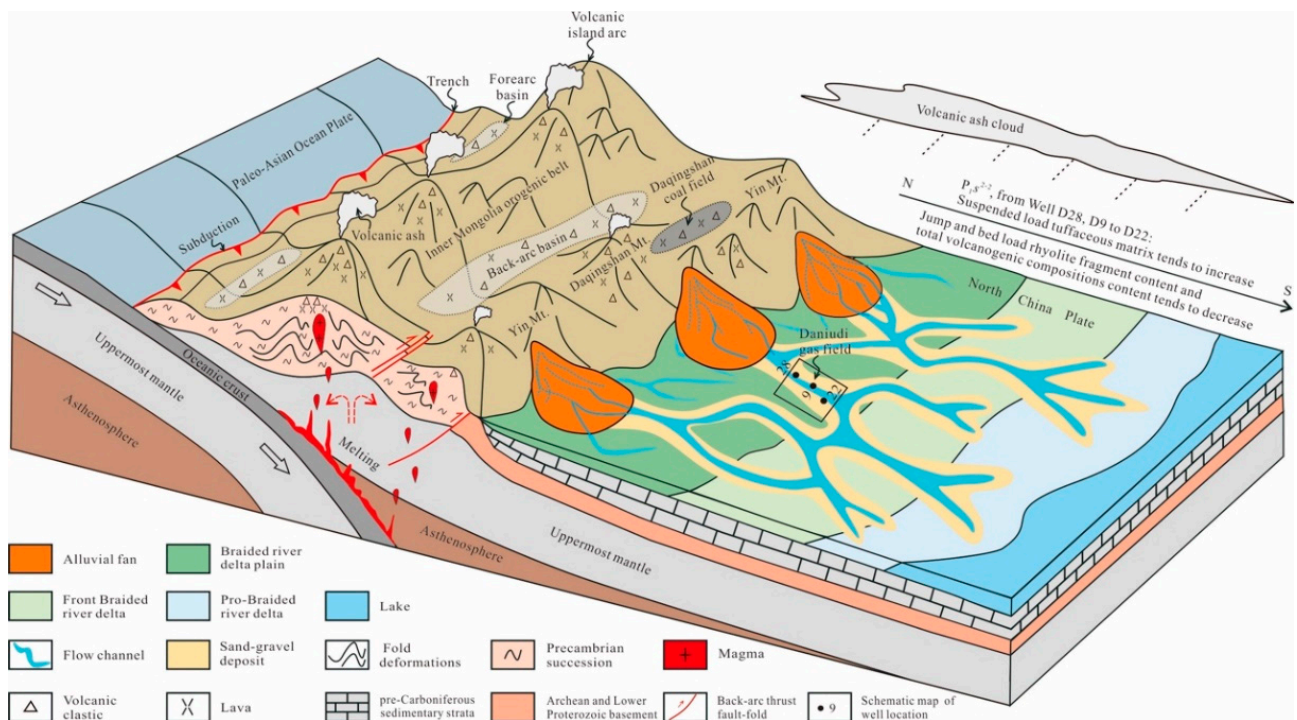


Figure 10. Tectonic-sedimentary model and provenance of the Shanxi Formation in the north of the Ordos Basin.

5.2.2. Provenance of the Volcanogenic Components

The Ordos Basin is located in the western part of the North China Plate, and there are few reports about the Late Paleozoic volcanic eruptions in the basin due to the absence of magmatic and tectonic activities. As mentioned above, large-scale, multi-episode, Late Carboniferous to Early Permian intermediate-acid volcanic eruptions were reported in the Inner Mongolia Orogenic Belt, located to the north of the Ordos Basin (Figures 1b and 9). The Tsagaannuur and Baolige Temple volcanic rock associations mainly consist of rhyolite, dacite, and andesite, which are distributed along the Sunit Right Banner-Linxi Tectonic Belt and East Ujimqin Banner Tectonic Belt (Figure 9) [13,95]. The isotopic age of these volcanic rocks mainly ranges from 320 Ma to 300 Ma and from 300 Ma to 290 Ma, which is consistent with the depositional period of the Shanxi Formation (295–298 Ma) [24]. The volcanogenic components in the Ordos Basin and North China Plate may be related to those volcanic eruptions.

However, the volcanic components of the Shanxi Formation are unlikely to directly originate from the Inner Mongolia Orogenic Belt for the following reasons. (1) As mentioned previously, the provenance of the Shanxi Formation was mainly attributed to the Yin Mountain (Yinshan Orogenic Belt or Yin Mountain uplift), which is located between the Ordos Basin and the Inner Mongolia Orogenic Belt. The Yin Mountain uplift in the Late Paleozoic prevented the transportation of materials from the Inner Mongolia Orogenic Belt into the basin (Figure 9). (2) There is a considerable distance of approximately 400 to 600 km between the Daniudi Gas Field and the Sunit Right Banner-Linxi Tectonic Belt or the East Ujimqin Banner Tectonic Belt (Figure 9). In general, sandstone with high compositional and structural maturity is conducive to long-distance transportation. Paradoxically, the main type of sandstone in the study area is lithic sandstone, followed by lithic greywacke (Table 1; Figure 3), and both sandstones contain large amounts of lithic fragments and tuffaceous matrix (Figure 2c,g–i and Figure 4c–l). Furthermore, the presence of volcanogenic quartz with partly embayed boundaries or angular shapes suggests a rapid sediment accumulation near the source (Figure 4a,b). (3) The Shanxi Formation in the Daniudi Gas Field is predominantly characterized by braided river delta plain deposits [73,74]. These

deposits were formed through a rapid accumulation process and were located close to the source region.

The most likely provenance of the volcanogenic components in the Shanxi Formation is the Daqingshan Mountain, which is located in the north of the Ordos Basin and is also situated in the middle of the Yinshan Mountain range (Figures 1b and 9). The Daqingshan coal field is situated on the southern slope of the Daqingshan Mountain (Figure 9) and spans approximately 70 km from east to west and 1 to 10 km from south to north. Over nine layers of volcanic event strata were discovered in the late Paleozoic coal-measure strata in the Daqingshan coal field, mainly consisting of welded tuff, volcanic breccia, ignimbrite, tuff, and sedimentary tuff (Figure 9) [82,96,97]. Notably, the total thickness of volcanic rock (excluding sedimentary pyroclastic rock and volcanoclastic sedimentary rocks) is approximately 42 m [97]. This finding suggests that a substantial amount of volcanic rock accumulated in the Daqingshan area, providing sufficient volcanic materials for the Daqingshan coal field and the Shanxi Formation in the Ordos Basin. Moreover, the accumulation of intermediate-acid volcanic materials in the Daqingshan area is consistent with the volcanogenic quartz, rhyolite fragments, tuff fragments, and tuffaceous matrix in the Shanxi Formation. Meanwhile, the isotopic age of the volcanic rocks in the Daqingshan area is 305 Ma [82], which is also consistent with the depositional period of the Shanxi Formation (295–298 Ma) [24]. In addition, the similar trace element spidergram shows that the Shanxi Formation has a strong affinity with the volcanic rocks in the Daqingshan area (Figure 5). More importantly, the distance between the Daniudi Gas Field and the Daqingshan area is approximately 120 km, which is ideal for the rapid accumulation of a braided river delta plain (Figure 9). Based on the above considerations, we believe that the volcanogenic components in the Shanxi Formation most likely derived from the Daqingshan area. The provenance of the Shanxi Formation in the Daniudi Gas Field was derived not only from the ancient land of the Yin Mountain but also from the accumulation of Late Carboniferous to Early Permian intermediate-acid volcanic materials in the Daqingshan area (Figure 10).

It is usually considered that the Late Carboniferous to Early Permian volcanic materials in the Daqingshan area mainly originated from volcanic eruptions in the Inner Mongolia Orogenic Belt and were transported through the air [28,96,101]. However, this study presents evidence of Late Carboniferous to Early Permian intermediate-acid volcanic eruptions occurring directly within the Daqingshan area (Figure 10). Firstly, the timing of volcanic material accumulation in the provenance (Daqingshan area) can be constrained by the age peaks of detrital zircons (301 Ma and 304 Ma) in the Shanxi Formation [13,87]. Furthermore, andesitic and dacitic welded tuff containing 20% of various tephra, as well as volcanic breccia characterized by poorly sorted, subangular tephra of rhyolite, dacite, and andesite, have been discovered in the Daqingshan coal field [82,96,97]. Welded tuff and lava breccia are the products of magma consolidation, which is close to the volcanic eruption centers. Additionally, the coarse volcanogenic quartz with partly embayed boundaries or angular shapes, as well as a coarse and high content of rhyolite fragments in the Shanxi Formation (Figure 4a–f), also indicate that the intermediate-acid volcanic eruption centers are located in or near the source area.

5.2.3. Transportation of the Volcanogenic Components

The volcanic ash layers in the Shanxi Formation, which were transported by air, could be well explained by contemporaneous volcanic activities. However, the volcanogenic components in each sub-layer of the Shanxi Formation were hard to be transported by air (Table 5). The intermittent volcanic activities and relatively short residence time in the air of volcanogenic materials could not have continuously and stably contributed to the provenance of the Shanxi Formation within 3 Ma for each sub-layer. Furthermore, the presence of coarse volcanogenic materials, such as coarse lava fragments exclusively in channels, and fine volcanogenic materials only could be found in a flood plain, implying that these materials are primarily transported by flowing water. Considering the paleocur-

rent directions of the Shanxi Formation in the study area, which were primarily from north to south or from northeast to southwest [102,103], the flowing water transportation also could be proved by the variation of volcanogenic component content from north to south. Taking the P_1s^{2-2} as an example, the content of saltation and bed load rhyolite fragments and the total content of volcanogenic components tend to gradually decrease, while the content of suspended load tuffaceous matrix tends to increase from Well 28 to Well 9 to Well 22 (Table 5; Figure 10). Therefore, these volcanogenic components in the Shanxi Formation were mainly transported by flowing water of alluvial fans and braided rivers rather than by air (Figure 10).

Table 5. Percentages of volcanogenic components for each sub-layer and typical wells of the Shanxi Formation in the Daniudi Gas Field (%).

Sub-layer/ Well	Samples	Rhyolite Fragment (%)			Tuff Fragment (%)			Tuffaceous Matrix (%)			Volcanogenic Components (%)		
		MIN	MAX	AVG	MIN	MAX	AVG	MIN	MAX	AVG	MIN	MAX	AVG
S2-2-2	5	5.0	10.0	8.2	4.0	8.0	6.0	3.0	13.0	8.0	12.0	31.0	22.2
S2-2-1	14	5.0	25.0	10.5	3.0	15.0	7.4	4.0	15.0	8.4	12.0	55.0	26.3
S2-1-2	2	13.0	15.0	14.0	5.0	10.0	7.5	7.0	8.0	7.5	25.0	33.0	29.0
S2-1-1	3	10.0	13.0	11.7	5.0	10.0	7.7	6.0	10.0	8.7	21.0	33.0	28.1
S1-3-2	5	5.5	18.0	12.7	3.0	15.0	7.0	5.5	12.0	8.7	14.0	45.0	28.4
S1-3-1	6	7.0	29.0	16.5	1.0	15.0	4.8	5.0	15.0	9.2	13.0	59.0	30.5
S1-2-2	4	8.0	15.0	11.3	1.0	5.0	2.8	8.0	10.0	9.5	17.0	30.0	23.5
S1-2-1	3	2.0	10.0	6.3	2.0	4.0	3.0	6.0	10.0	8.3	10.0	24.0	17.6
S1-1-2	2	10.0	20.0	15.0	4.0	5.0	4.5	4.0	8.0	6.0	18.0	33.0	25.5
S1-1-1	5	2.0	20.0	9.2	2.0	7.0	3.8	4.0	12.0	7.6	8.0	39.0	20.6
28	4	15.0	35.0	22.0	3.0	10.0	6.1	5.0	10.0	8.3	31.0	43.5	36.4
9	6	5.0	20.0	12.8	5.0	12.0	7.9	5.0	15.0	8.8	23.0	35.0	29.9
22	5	4.0	18.0	8.6	2.0	10.0	5.0	6.0	13.0	10.6	18.0	32.0	24.2

MIN: minimum; MAX: maximum; AVG: average.

5.3. Tectonic Implications of High Content Volcanogenic Components in the Shanxi Formation

The northern margin of the North China Plate is a key region for exploring the evolution of the Xing-Meng Orogenic Belt and the closure of the Paleo-Asian Ocean. The subduction direction of the plate in the Xing-Meng Orogenic Belt during the Late Carboniferous to Early Permian and the closure time of the Paleo-Asian Ocean are still discussed. Some researchers believe that the North China Plate subducted northward beneath the Southern Mongolian Microcontinent of the Siberia Plate [27–29], while others insist that the Paleo-Asian Ocean Plate subducted southward beneath the northern margin of the North China Plate [11,31,32,101,104]. In addition, it is argued that the Paleo-Asian Ocean closed in the Late Devonian to Early Carboniferous [33–36] or in the Late Permian to Early Triassic [37–41]. The Late Carboniferous to Early Permian intermediate-acid volcanic eruptions in the Daqingshan area could help us better understand the tectonic evolution of this area from a new point of view.

First of all, the Late Carboniferous to Early Permian intermediate-acid magmatic activities could extend southward to the northern margin of the North China Plate from the Inner Mongolia Orogenic Belt (Figure 9). The spatial distribution of magmatism related to the subduction of plates is no longer limited to the Inner Mongolia Orogenic Belt. However, it is important to note that the scale of magmatic activities significantly varies between the northern margin of the North China Plate and the Inner Mongolia Orogenic Belt. The thickness of the Tsagaannuur (C_2), Baolige Temple (C_2), and Dashizhai (P_1) volcanic rock associations in the Inner Mongolia Orogenic Belt is 1990~2089 m, ca. 2400 m, and 1150~2000 m, respectively [95]. While the total thickness of the Shuanmazhuang Formation (C_2), Zahuaigou Formation (C_2), and Shiyewan Zahuaigou Formation (C_2) in the Daqingshan area is 250~350 m, there are 39 layers of volcanic event deposits interbedded [28,101]. Clearly, the scale of magmatic activity in the Daqingshan area is much weaker than that

in the Inner Mongolia Orogenic Belt, and the scale tends to decrease dramatically from north to south. This suggests that those volcanic activities were triggered by the southward subduction of the Paleo-Asian Ocean Plate, and the northern part of the North China Plate could also be affected by the magmatic activities related to the subduction in the Late Carboniferous to Early Permian. This conclusion is further supported by the Dickinson plots of clastic components in sandstones (Figure 7) and the plots of Th-Sc-Zr/10 and La-Th-Sc (Figure 8), which indicate an active continental margin with a trench–arc–basin system developed in the Late Carboniferous to Early Permian. Additionally, the high content of rhyolite and intermediate-acid ash accumulated in the provenance is also more likely to be consistent with a volcanic island arc setting. Therefore, the active continental margin related to the subduction of the Paleo-Asian Ocean Plate lasted at least until the Early Permian, and the complete closure of the Paleo-Asian Ocean must have occurred later than the Early Permian.

6. Conclusions

(1) A high content of volcanogenic components was discovered in the Shanxi Formation of the Daniudi Gas Field, with the average contents of volcanogenic components exceeding 27.6%. The volcanogenic components include volcanogenic quartz, lava fragments (dominated by various kinds of rhyolite fragments), tuff fragments, and tuffaceous matrix, with average contents of approximately 5%, 11.5%, 5.4%, and 8.2%, respectively. In addition, at least two volcanic ash layers were discovered.

(2) The provenance of the Shanxi Formation in the Daniudi Gas Field was derived not only from older sources but also from much younger volcanic eruptions. It derived from the metamorphic rocks of the Precambrian succession of the Yin Mountain's ancient land that were part of an active recycled-orogenic setting, while the volcanogenic components most likely derived from younger intermediate-acid volcanic materials accumulated in the Daqingshan area in the Late Carboniferous to Early Permian, earlier or simultaneously with the deposition of the Shanxi Formation. The volcanogenic components in the Shanxi Formation were primarily transported by flowing water rather than by air from the source area to the basin.

(3) The Late Carboniferous to Early Permian intermediate-acid magmatic activities could have extended southward to the north margin of the North China Plate from the Inner Mongolia Orogenic Belt. The volcanic materials that accumulated in the Daqingshan area were associated with volcanic eruptions exclusive to this region. This phenomenon can be attributed to the southward subduction of the Paleo-Asian Ocean Plate beneath the northern margin of the North China Plate during the Late Carboniferous to Early Carboniferous period. The active continental margin related to the subduction of the Paleo-Asian Ocean Plate lasted at least until the Early Permian, and the closure of the Paleo-Asian Ocean must have occurred later than the Early Permian.

Author Contributions: Conceptualization, X.Q. and D.W.; methodology, X.Q., J.L., and H.C.; software, X.G.; validation, X.T., L.L., and J.W.; formal analysis, H.C. and W.Z.; investigation, X.Q., J.W., W.Z., and Q.W.; resources, T.L.; data curation, Q.W.; writing—original draft preparation, X.Q. and Q.W.; writing—review and editing, X.T., W.J., and T.L.; visualization, N.J.; supervision, D.W. and X.T.; project administration, D.W.; funding acquisition, X.Q. All authors have read and agreed to the published version of the manuscript.

Funding: This work is supported by the National Natural Science Foundation of China (Grant Numbers. 42102135, 42102133, 42072140), and Science and Technology Research Program of Chongqing Municipal Education Commission (Grant Numbers. KJQN202101535). Chongqing Outstanding Youth Scientist Fund project (Grant Numbers. CSTB2022NSCQ-JQX0031). Science and Technology major Research Program of Chongqing Education Commission (Grant Numbers. KJZD-M202101502).

Data Availability Statement: Data are contained within the article.

Conflicts of Interest: The authors declare no conflict of interest. Author Tao Lei was employed by the company North China Branch Company of SINOPEC. The remaining authors declare that the

research was conducted in the absence of any commercial or financial relationships that could be construed as a potential conflict of interest.

References

1. Yang, Z.; He, S.; Zou, C.N.; Li, Q.Y.; Chen, Z.Y. Coupling relationship between reservoir diagenesis and natural gas accumulation of Daniudi Gas Field in North Ordos Basin. *Acta Pet. Sin.* **2010**, *31*, 373–378, 385.
2. Wang, Z.; Zheng, M. Potash-forming regularity of the Ordovician marine northern Shaanxi salt basin: Insight from review and prospect of the deep geology of the Ordos basin. *Acta Geol. Sin.* **2018**, *92*, 1627–1644. [[CrossRef](#)]
3. Zhang, S.H.; Zhao, Y.; Song, B.; Yang, Z.Y.; Hu, J.M.; Wu, H. Carboniferous granitic plutons from the northern margin of the North China block: Implications for a late Paleozoic active continental margin. *J. Geol. Soc.* **2007**, *164*, 451–463. [[CrossRef](#)]
4. Li, Z.H.; Qu, H.J.; Gong, W.B. Late Mesozoic basin development and tectonic setting of the northern North China Craton. *J. Asian Earth Sci.* **2015**, *114*, 115–139. [[CrossRef](#)]
5. Sengör, A.M.C.; Natal'in, B.A. Turkeic-type orogeny and its role in the making of the continental crust. *Annu. Rev. Earth Planet. Sci.* **1996**, *24*, 263–337. [[CrossRef](#)]
6. Windley, B.F.; Alexeiev, D.; Xiao, W.J.; Kröner, A.; Badarch, G. Tectonic models for accretion of the Central Asian Orogenic Belt. *J. Geol. Soc.* **2007**, *164*, 31–47. [[CrossRef](#)]
7. Jahn, B.; Brian, W.; Boris, N.; Nick, D. Phanerozoic continental growth in central Asia—Preface. *J. Asian Earth Sci.* **2004**, *23*, 599–603. [[CrossRef](#)]
8. Guo, F.; Fan, W.M.; Miao, L.C.; Zhao, L. Early Paleozoic subduction of the Paleo-Asian Ocean: Geochronological and geochemical evidence from the Dashizhai basalts, Inner Mongolia. *Sci. China (Ser. D Earth Sci.)* **2009**, *52*, 940–951. [[CrossRef](#)]
9. Liu, R.E.; Huang, Y.M.; Wei, X.F.; Sun, F.J.; Lin, J. Analysis of provenance of Late Paleozoic in the Northern Ordos Basin and its geological significance. *J. Mineral. Petrol.* **2003**, *23*, 82–86.
10. Chen, A.Q.; Chen, H.D.; Xiang, F.; Liu, W.J.; Hou, Z.J.; Shang, Y.Z.; Ye, L.M.; Li, H. Sandstone characteristic and provenance analysis of the Permian Shanxi Formation-Shangshihezi Formation in the northeast of Ordos Basin, China. *J. Chengdu Univ. Technol. (Sci. Technol. Ed.)* **2007**, *34*, 305–311.
11. Chen, Q.H.; Li, W.H.; Liu, H.W.; Li, K.Y.; Pang, J.G.; Guo, Y.Q.; Yuan, Z. Provenance analysis of sandstone of the Upper Carboniferous to Middle Permian in Ordos Basin. *J. Palaeogeogr.* **2009**, *11*, 629–640.
12. Chen, Q.H.; Li, W.H.; Hu, X.L.; Li, K.Y.; Pang, J.G.; Guo, Y.Q. Tectonic setting and provenance analysis of Late Paleozoic sedimentary rocks in the Ordos Basin. *Acta Geol. Sin.* **2012**, *86*, 1150–1612.
13. Qu, H.J.; Han, X.; Chen, S.; Yang, B.; Du, M.Y.; Dong, Y.Y.; Zhao, C. U-Pb Dating of Detrital Zircon from the Upper Paleozoic Clastic Rocks and Basin-mountain Coupling of the Northeastern Ordos Basin. *Geotecton. Metallog.* **2020**, *44*, 501–513.
14. Dickinson, W.R.; Beard, S.; Brakenridge, R.; Erjavec, J.L.; Ferguson, R.C.; Inman, K.F.; Knepp, R.A.; Lindberg, A.; Ryberg, P.T. Provenance of North American Phanerozoic sandstones in relation to tectonic settings. *Geol. Soc. Am. Bull.* **1983**, *94*, 222–235. [[CrossRef](#)]
15. Schieber, J.A. Combined petrographical-geochemical provenance study of the Newland Formation, mid-Proterozoic of Montana. *Geol. Mag.* **1992**, *129*, 223–237. [[CrossRef](#)]
16. McCann, T. Sandstone composition and provenance of the Rotliegend of the NE German Basin. *Sediment. Geol.* **1998**, *116*, 177–198. [[CrossRef](#)]
17. Condie, K.C.; Lee, D.; Farmer, L. Tectonic setting and provenance of the Neoproterozoic Uinta Mountain and Big Cottonwood groups, northern Utah: Constraints from geochemistry, Nd isotopes, and detrital modes. *Sediment. Geol.* **2001**, *141–142*, 443–464. [[CrossRef](#)]
18. Arribas, J.; Alonso, A.; Mas, R.; Tortosa, A.; Rodas, M.; Barrenechea, J.; Alonso-Azcárate, J.; Artigas, R. Sandstone petrography of continental depositional sequences of an intraplate rift basin: Western Cameros Basin (North Spain). *J. Sediment. Res.* **2003**, *73*, 309–327. [[CrossRef](#)]
19. Osa, S.; Asiedu, D.K.; Banoeng-Yakubo, B.; Koeberl, C.; Dampare, S.B. Provenance and tectonic setting of late Proterozoic Buem sandstones of southeastern Ghana: Evidence from geochemistry and detrital modes. *J. Afr. Earth Sci.* **2006**, *44*, 85–96. [[CrossRef](#)]
20. Ciccio, P.L.; Limarino, C.O.; Isbell, J.L.; Taboada, A.C.; Pagani, M.A.; Gulbranson, E.L. Interpreting detrital modes and geochemistry of sandstones from the late Paleozoic Tepuel-Genoa Basin: Paleogeographic implications (Patagonia, Argentina). *J. S. Am. Earth Sci.* **2020**, *104*, 102858. [[CrossRef](#)]
21. Darby, B.J.; Ritts, B.D. Mesozoic contractional deformation in the middle of the Asian tectonic collage: The intraplate Western Ordos fold-thrust belt, China. *Earth Planet Sci. Lett.* **2002**, *205*, 13–24. [[CrossRef](#)]
22. Xu, N.N.; Qiu, L.W.; Eriksson, K.A.; Klyukin, Y.I.; Wang, Y.; Yang, Y.Q. Influence of detrital composition on the diagenetic history of tight sandstones with implications for reservoir quality: Examples from the Permian Xiashihezi Formation and Carboniferous Taiyuan Formation, Daniudi gas field, Ordos Basin, China. *Mar. Pet. Geol.* **2017**, *88*, 756–784. [[CrossRef](#)]
23. Yang, Y.; Li, W.; Ma, L. Tectonic and stratigraphic controls of hydrocarbon systems in the Ordos basin: A multicycle cratonic basin in central China. *AAPG Bull.* **2005**, *89*, 255–269. [[CrossRef](#)]
24. Shen, B.H.; Shen, S.W.; Wu, Q.; Zhang, S.C.; Zhang, B.; Wang, X.D.; Hou, Z.S.; Yuan, D.X.; Zhang, Y.C.; Liu, F.; et al. Carboniferous and Permian integrative stratigraphy and timescale of North China Block. *Sci. China (Earth Sci.)* **2022**, *65*, 983–1011. [[CrossRef](#)]

25. Cohen, K.M.; Finney, S.C.; Gibbard, P.L.; Fan, J.-X. The ICS International Chronostratigraphic Chart. *Episodes* **2023**, *36*, 199–204. [[CrossRef](#)] [[PubMed](#)]
26. Tan, C.X.; Li, W.H.; Feng, J.P.; Zeng, M.; Bu, Y. Analysis of sedimentary source of reservoir in Daniudi Gas Field in Ordos Basin. *Acta Mineral. Sin.* **2010**, *30*, 389–397.
27. Shang, G.X. An outline of basining structures of North China Late Palaeozoic coal accumulation basin. *Coal Geol. China* **1995**, *30*, 17, 1–6.
28. Zhou, A.C. *The Evolution of Late Paleozoic Basins in North Margin of North China Block and the Coupling Relationship between Basin and Range*; Northwestern University: Xi'an, China, 2000.
29. Shao, J.A.; Tang, K.D.; He, G.Q. Early Permian tectono-palaeogeographic reconstruction of Inner Mongolia, China. *Acta Petrol. Sin.* **2014**, *7*, 1858–1866.
30. Chen, B.; Jahn, B.M.; Tian, W. Evolution of the Solonker suture zone: Constraints from zircon U–Pb ages, Hf isotopic ratios and whole-rock Nd–Sr isotope compositions of subduction- and collision-related magmas and forearc sediments. *J. Asian Earth Sci.* **2009**, *34*, 245–257. [[CrossRef](#)]
31. Zhao, Y.; Zhai, M.G.; Chen, H.; Zhang, S.H. Paleozoic-Early Jurassic tectonic evolution of North China Craton and its adjacent orogenic belts. *Geol. China* **2017**, *44*, 44–60.
32. Chen, A.Q.; Zhou, H.; Ogg, J.G.; Yang, S.; Hou, M.C.; Jiang, X.W.; Xu, S.L.; Zhang, X.X. Source-to-sink of Late carboniferous Ordos Basin: Constraints on crustal accretion margins converting to orogenic belts bounding the North China Block. *Geosci. Front.* **2020**, *11*, 2031–2052. [[CrossRef](#)]
33. Xu, B.; Chen, B. The structure and evolution of Paleozoic -Mesozoic orogenic belt between North China Plate and Siberian Platein northern Inner Mongolia. *Sci. China (Ser. D)* **1997**, *27*, 227–232.
34. Shao, J.A.; Tian, W.; Tang, K.D. Petrogenesis and tectonic settings of the Late Carboniferous high Mg basalts of Inner Mongolia. *Earth Sci. Front.* **2015**, *22*, 171–181.
35. Zhu, J.B.; Ren, J.S. Carboniferous-Permian Stratigraphy and Sedimentary Environment of Southeastern Inner Mongolia, China: Constraints on Final Closure of the Paleo-Asian Ocean. *Acta Geol. Sin.* **2017**, *91*, 832–856. [[CrossRef](#)]
36. Tong, Y. Giant late Carboniferous-early Permian alkaline granite belt along the China and Mongolia Border and its implication for the evolution of the CAOB. *Geophys. Res. Abstr.* **2019**, *21*, 1.
37. Sengör, A.M.C.; Natal'in, B.A.; Burtman, V.S. Evolution of the Altaid tectonic collage and Palaeozoic crustal growth in Eurasia. *Nature* **1993**, *364*, 299–307. [[CrossRef](#)]
38. Xiao, W.J.; Windley, B.F.; Hao, J.; Zai, N.G. Accretion leading to collision and the Permian Solonker suture, Inner Mongolia, China: Termination of the Central Asian orogenic belt. *Tectonics* **2003**, *22*, 1069–1089. [[CrossRef](#)]
39. Li, J.Y.; Wang, K.Z.; Sun, G.H.; Mo, S.G.; Li, W.Q.; Yang, T.N.; Gao, L.M. Paleozoic active margin slices in the southern Turfan-Hami basin: Geological records of subduction of the Paleo-Asian Ocean plate in central Asian regions. *Acta Petrol. Sin.* **2006**, *22*, 1087–1102.
40. Meng, Q.P.; He, Y.K.; Zhang, W.; Wu, T.R.; Zheng, R.G.; Xu, C.; Zhang, Z.Y. Time constraints on the closure of the Paleo-Asian Ocean on the northern margin of North China Craton: Evidence from Xihouhaozisyen-collisional granites in Siziwang Qi area. *Geol. Bull. China* **2013**, *32*, 1749–1759.
41. Yi, X.C.; Ye, G.F.; Jin, S.; Wei, W.B. Constraints on the process and mode of the Paleo-Asian Ocean closure from the lithospheric conductivity structure of the south-eastern Central Asian Orogenic Belt. *Tectonophysics* **2022**, *838*, 229485. [[CrossRef](#)]
42. Dai, J.X.; Li, J.; Luo, X.; Zhang, W.; Hu, G.; Ma, C.; Guo, J.; Ge, S. Stable carbon isotope compositions and source rock geochemistry of the giant gas accumulations in the Ordos Basin, China. *Org. Geochem.* **2005**, *36*, 1617–1635. [[CrossRef](#)]
43. Yuan, Z.X. *On Upper Paleozoic Subtle Gas Pools in Tabamiao District*; Chengdu University of Technology: Chengdu, China, 2005.
44. Hou, Z.S.; Chen, S.Y.; Liang, Z. Sedimentary features and sequence stratigraphy of the successions around the Carboniferous-Permian boundary in the Ordos Basin: Links to glacial and volcanic impacts. *J. Palaeogeogr.* **2023**, *12*, 358–383. [[CrossRef](#)]
45. Li, R.X.; Li, Y.Z. Tectonic evolution of the western margin of the Ordos Basin (Central China). *Russ. Geol. Geophys.* **2008**, *49*, 23–27.
46. Li, Y.; Tang, D.Z.; Wu, P.; Niu, X.L.; Wang, K.; Qiao, P. Continuous unconventional natural gas accumulations of Carboniferous-Permian coal-bearing strata in the Linxing area, northeastern Ordos basin, China. *J. Nat. Gas Sci. Eng.* **2016**, *36*, 314–327. [[CrossRef](#)]
47. Yang, M.H.; Liu, C.Y.; Lan, C.L.; Liu, L.; Li, X.; Zhang, K.S. Late Carboniferous-Early Permian sequence stratigraphy and depositional evolution in the Northeast Ordos Basin, North China. *Acta Geol. Sin. (Engl. Ed.)* **2010**, *84*, 1220–1228.
48. Wang, M.J.; He, D.F.; Bao, H.P.; Lu, R.Q.; Gui, B.L. Upper Palaeozoic gas accumulations of the Yimeng uplift, Ordos Basin. *Pet. Explor. Dev.* **2011**, *38*, 30–39.
49. Changqing Oil Field Petroleum Geology Editorial Committee. *Petroleum Geology of China (Vol. 12) Changqing Oil Field*; Petroleum Industry Press: Beijing, China, 1992.
50. Li, P.W.; Gao, R.; Guan, Y.; Li, Q.S. The Closure Time of the Paleo-Asian Ocean and the Paleo-Tethys Ocean: Implication for the Tectonic Cause of the End-Permian Mass Extinction. *J. Jilin Univ. (Earth Sci. Ed.)* **2009**, *39*, 521–527.
51. Wilhem, C.; Windley, B.F.; Stampfli, G.M. The Altaids of Central Asia: A tectonic and evolutionary innovative review. *Earth-Sci. Rev.* **2012**, *113*, 303–341. [[CrossRef](#)]
52. Li, J.Y.; Zhang, J.; Yang, T.N.; Li, Y.P.; Sun, G.H.; Zhu, Z.X.; Wang, L.J. Crustal tectonic division and evolution of the southern part of the North Asian Orogenic Region and its adjacent areas. *J. Jilin Univ. (Earth Sci. Ed.)* **2009**, *39*, 584–605.

53. Zhang, S.H.; Zhao, Y.; Ye, H.; Liu, J.M.; Hu, Z.C. Origin and evolution of the Bainaimiao arc belt: Implications for crustal growth in the southern Central Asian orogenic belt. *Geol. Soc. Am. Bull.* **2014**, *126*, 1275–1300. [[CrossRef](#)]
54. Ma, S.X.; Meng, Q.R.; Qu, Y.Q. A study of detrital zircons of Late Carboniferous–Middle Triassic strata in the northern margin of North China block and its geological implication. *Geol. Bull. China* **2011**, *30*, 1485–1500.
55. Zhao, Y.; Chen, B.; Zhang, S.H.; Liu, J.M.; Hu, J.M.; Liu, J.; Fei, J.L. Pre-Yanshanian geological events in the northern margin of the North China Craton and its adjacent areas. *Geol. China* **2010**, *37*, 900–915.
56. Ma, Q.L.; Xu, X.R.; Du, Y.S. Zircon U–Pb Chronology and Provenance of the Sanhao Conglomerate in Zhoukoudian, Beijing: Implications for Coeval Paleogeography. *Geol. Sci. Info. Technol. Info.* **2017**, *36*, 29–35.
57. Liu, J.; Zhao, Y.; Liu, A.; Zhang, S.; Yang, Z.; Zhou, S. Origin of Late Palaeozoic bauxites in the North China Craton: Constraints from zircon U–Pb geochronology and in situ Hf isotopes. *J. Geol. Soc.* **2014**, *171*, 695–707. [[CrossRef](#)]
58. Zhang, S.H.; Zhao, Y.; Liu, J.M.; Hu, Z.C. Different sources involved in generation of continental arc volcanism: The Carboniferous–Permian volcanic rocks in the northern margin of the North China block. *Lithos* **2016**, *240*, 382–401. [[CrossRef](#)]
59. Zhang, S.H.; Zhao, Y.; Song, B. Hornblende thermobarometry of the Carboniferous granitoids from the Inner Mongolia Paleoplift: Implications for the tectonic evolution of the northern margin of North China block. *Mineral. Petrol.* **2006**, *87*, 123–141. [[CrossRef](#)]
60. Cope, T.D.; Shultz, M.R.; Graham, S.A. Detrital record of Mesozoic shortening in the Yanshan belt, NE China: Testing structural interpretations with basin analysis. *Basin Res.* **2007**, *19*, 253–272. [[CrossRef](#)]
61. Zhang, S.H.; Zhao, Y.; Song, B.; Yue, H.Y. Zircon SHRIMP U–Pb and in-situ Lu–Hf isotope analyses of a tuff from Western Beijing: Evidence for missing Late Paleozoic arc volcano eruptions at the northern margin of the North China block. *Gondwana Res.* **2007**, *12*, 157–165. [[CrossRef](#)]
62. Xiao, W.J.; Widley, B.F.; Huang, B.C.; Han, C.M.; Yuan, C.; Chen, H.L.; Sun, M.; Sun, S.; Li, J.L. End-Permian to mid-Triassic termination of the accretionary processes of the southern Altaids: Implications for the geodynamic evolution, Phanerozoic continental growth, and metallogeny of Central Asia. *Int. J. Earth Sci.* **2009**, *98*, 1189–1217. [[CrossRef](#)]
63. Zhang, S.H.; Zhao, Y.; Kröner, A.; Liu, X.M.; Xie, L.W.; Chen, F.K. Early Permian plutons from the northern North China Block: Constraints on continental arc evolution and convergent margin magmatism related to the Central Asian Orogenic Belt. *Int. J. Earth Sci.* **2009**, *98*, 1441–1467. [[CrossRef](#)]
64. Eizenhöfer, P.R.; Zhao, G.; Zhang, J.; Sun, M. Final closure of the Paleo-Asian Ocean along the Solonker suture zone: Constraints from geochronological and geochemical data of Permian volcanic and sedimentary rocks. *Tectonics* **2014**, *33*, 441–463. [[CrossRef](#)]
65. Zhang, S.H.; Zhao, Y.; Song, B.; Hu, J.M.; Liu, S.W.; Yang, Y.H.; Chen, F.K.; Liu, X.M.; Liu, J. Contrasting Late Carboniferous and Late Permian–Middle Triassic intrusive suites from the northern margin of the North China craton: Geochronology, petrogenesis, and tectonic implications. *Geol. Soc. Am. Bull.* **2009**, *121*, 181–200. [[CrossRef](#)]
66. Ren, Z.L. Thermal history of Ordos Basin assessed by apatite fission track analysis. *Acta Geophys. Sin.* **1995**, *38*, 339–349.
67. Zhao, M.W.; Behr, H.J. Vitrinite reflectance in Triassic with relation to geothermal history of Ordos Basin. *Acta Pet. Sin.* **1996**, *17*, 15–23.
68. Yang, J.J.; Pei, X.G. *Chinese Natural Gas Geology, Volume 4, Ordos Basin*; Petroleum Industry Press: Beijing, China, 1996.
69. Wang, T.H. Structural styles of fronts of thrust-detachment faults in petroleum-bearing areas of Western China. *Acta Geol. Sin.* **1999**, *73*, 371–383.
70. Bradley, D.R.; Andrew, D.H.; Brian, J.D.; Lynde, N.; Adrian, B. Sedimentary record of Triassic intraplate extension in North China: Evidence from the nonmarine NW Ordos Basin, Helan Shan and Zhuozi Shan. *Tectonophysics* **2004**, *386*, 177–202.
71. Bradley, D.R.; Amy, W.; Stephan, A.G.; Brian, J.D. Mesozoic tectonics and sedimentation of the giant polyphase nonmarine intraplate Ordos Basin, western North China Block. *Int. Geol. Rev.* **2009**, *51*, 95–115.
72. Hou, R.Y.; Liu, Z.Q. Reservoir evaluation and development strategies of Daniudi tight sand gas field in the Ordos Basin. *Oil Gas Geol.* **2012**, *33*, 118–128.
73. Tan, C.X.; Li, W.H.; Zhang, H.J.; Zheng, Y. Study of the sedimentary facies of Shanxi formation in Daniudi Gasfield of Ordos Basin. *J. Northwest Univ. (Nat. Sci. Ed.)* **2011**, *41*, 107–112.
74. Wan, Y.L.; Li, Z.D.; Peng, C.; Kong, W.; Xie, Y.X.; Zheng, T. Reservoir characteristics and evaluation of low porosity and permeability sandstone of member of Shanxi Formation in Daniudi Gas Field, Ordos Basin. *J. Mineral. Petrol.* **2016**, *36*, 106–114.
75. Zhang, Q.; Bai, J.F.; Wang, Y. Analytical scheme and quality monitoring system for China Geochemical Baseline. *Earth Sci. Front.* **2012**, *19*, 33–42.
76. Folk, R.L. *Petrology of Sedimentary Rocks*; Hemphill Publishing Company: Austin, TX, USA, 1974.
77. Wang, J.W.; Bao, Z.D.; Chen, M.J.; Sun, F.J.; Liu, R.E.; Zhao, M.F.; Sun, Q.Y. Differentiation of sandstones’ tuff fillings and its effect on porosity—An example from the Paleozoic sandstones in Northwestern Ordos. *Chin. J. Geol.* **2005**, *40*, 429–438, 456.
78. Li, X.B.; Wang, J.W. The formation and evolution of volcanic dust fillings of sandstone in coal measures strata of Ordos Basin. *Acta Petrol. Mineral.* **2007**, *26*, 42–48.
79. Bhatia, M.R. Plate tectonics and geochemical composition of sandstones. *J. Geol.* **1981**, *91*, 611–627. [[CrossRef](#)]
80. Bhatia, M.R.; Crook, K.A.W. Trace element characteristics of graywackes and tectonic setting discrimination of sedimentary basins. *Contrib. Mineral. Petrol.* **1986**, *92*, 181–193. [[CrossRef](#)]
81. Taylor, S.R.; McLennan, S.M. *The Continental Crust: Its Composition and Evolution*; Blackwell Scientific Publications: Oxford, UK, 1985.

82. Zhang, Q.; Li, Y.H.; Chen, G.C.; Han, W.; Wang, J. Geochronology, geochemistry, and Hf isotopic compositions of the Late-Carboniferous volcanic rocks in Tongshengmao of Daqinshan area, Inner Mongolia and their geological implications. *Geol. J. China Univ.* **2018**, *24*, 160–171.
83. Duan, R.H. *The Nature and Significance of the Late Neoproterozoic and Late Paleoproterozoic Tectono-Thermal Events in the Southern Margin of the Yinshan Block of the North China Craton*; Chinese Academy of Geological Sciences: Beijing, China, 2021.
84. Norry, M.J.; Dunham, A.C.; Hudson, J.D. Mineralogy and geochemistry of the Peterborough Member, Oxford Clay Formation, Jurassic, UK: Element fractionation during mudrock sedimentation. *J. Geol. Soc.* **1994**, *151*, 195–207. [[CrossRef](#)]
85. Dickinson, W.R.; Suczek, C.A. Plate tectonics and sandstone compositions. *AAPG Bull.* **1979**, *63*, 2164–2182.
86. Zai, Y.S.; Deng, J.; Tang, Z.L.; Xiao, R.G.; Song, H.L.; Peng, R.M.; Sun, Z.S.; Wang, J.P.; Xiang, Y.C.; Huang, H.S.; et al. *Metallogenic System of Ancient Land Margin*; Geological Publishing House: Beijing, China, 2002.
87. Chen, B. *The U-Pb Geochronology of Detrital Zircon and Its Geological Significance of the Upper Paleozoic in the Northeastern Ordos Basin*; Northwest University: Xi'an, China, 2020.
88. Shao, L.; Liu, Z.W.; Zhu, W.L. Application of sedimentary geochemistry of terrigenous classic rock to basin analysis. *Earth Sci. Front.* **2000**, *7*, 297–304.
89. Yang, J.H.; Wu, F.Y.; Shao, J.A.; Wilde, S.; Xie, L.W.; Liu, X.M. Constraints on the timing of uplift of the Yanshan Fold and Thrust Belt, North China. *Earth Planet. Sci. Lett.* **2006**, *246*, 336–352. [[CrossRef](#)]
90. Zhu, X.Q.; Zhu, W.B.; Ge, R.F.; Wang, X. Late Paleozoic provenance shift in the south-central North China Craton: Implications for tectonic evolution and crustal growth. *Gondwana Res.* **2014**, *25*, 383–400. [[CrossRef](#)]
91. Luo, S.S.; Pan, Z.Y.; Lv, Q.Q.; He, W.L.; Wen, S. The Upper Paleozoic detrital zircon U-Pb geochronology and its tectonic significance in southwestern Ordos Basin. *Geol. China* **2017**, *44*, 556–574.
92. Sun, J.; Yang, L.; Dong, Y.; Yang, X.; Peng, Y.; Zhao, J. Permian tectonic evolution of the southwestern Ordos Basin, North China: Integrating constraints from sandstone petrology and detrital zircon geochronology. *Geol. J.* **2020**, *55*, 8068–8091. [[CrossRef](#)]
93. Hu, J.L.; Wang, L.L.; Chen, Q.; Huang, D.J.; Liu, L.; Zhang, J.Q.; Wang, Z.W.; Zhu, S.Z. The Early-Middle Permian source to sink filling process and its tectonic-sedimentary response in the southwestern Ordos Basin. *Nat. Gas Geosci.* **2023**, *12*, 1–25.
94. Wang, F.; Liu, X.S.; Zhao, W.B.; Zhang, L.; Hu, J.L.; Tian, J.C.; Chen, R.; Wang, J.; Wu, J.Y.; Xiao, Y.X. Detrital Zircon U-Pb Geochronology Characteristics of Permian Sandstone and Its Constraints on the Tectonic Evolution of the Southern Ordos Basin. *Acta Sedimentol. Sin.* **2023**, *41*, 1396–1413.
95. Bureau of Geology and Mineral Resources of Inner Mongolia Autonomous Region. *Regional Geology of Inner Mongolia Autonomous Region, People's Republic of China, Ministry of Geology and Mineral Resources, Geological Memoirs*; Geological Publishing House: Beijing, China, 1991.
96. Jia, B.W.; Zhou, A.C.; Guo, M.T. Study on the provenance of the Late Paleozoic volcanic events in Daqingshan area. *Chin. Sci. Abstr.* **1999**, *5*, 506–510.
97. Zhou, A.C.; Jia, B.W.; Ma, M.L.; Zhang, H. The Whole Sequences of Volcanic Event Deposits on the North Margin of the North China Plate and Their Features. *Geol. Rev.* **2001**, *47*, 175–183.
98. Li, M.P.; Shao, L.Y.; Li, Z.X.; Dong, D.X.; Li, J.Q. Lithofacies palaeogeography of lower coal group accumulation period of Carboniferous-Permian in North China. *J. China Coal Soc.* **2020**, *45*, 2399–2410.
99. Zhai, Y.H.; He, D.F.; Kai, B.Z. Tectono-depositional environment and prototype basin evolution in the Ordos Basin during the Early Permian. *Earth Sci. Front.* **2023**, *30*, 139–153.
100. Quan, X.Y. *Paleozoic Geological Structure Characteristics, Its Evolution and Oil and Gas Occurrence in Yimeng Uplift and Its Surrounding Areas*; Northwest University: Xi'an, China, 2020.
101. Jia, B.W.; Wu, Y.Q. The provenance and stratigraphic significance of volcanic event layers in Late Paleozoic coal measures from Daqingshan, Inner Mongolia. *J. Geol. Min. Res. North China* **1995**, *10*, 203–213.
102. Liu, W.B.; Chen, Y.T.; Wang, D.Y.; Zheng, C.G.; Huang, G. Study on the characteristics of palaeocurrents by using dipmeter logging data. *Sci. Geol. Sin.* **1994**, *29*, 291–297.
103. Lin, X.X. *A Synthetic Thought of Provenance Analysis in the Terrigenous Clastic Rock Basin—An Example in the Lower Permian Shanxi Formation, Northern Ordos Basin*; Chengdu University of Technology: Chengdu, China, 2011.
104. Li, J.Y. Permian geodynamic setting of Northeast China and adjacent regions: Closure of the Paleo-Asian Ocean and subduction of the Paleo-Pacific Plate. *J. Asian Earth Sci.* **2006**, *26*, 207–224. [[CrossRef](#)]

Disclaimer/Publisher's Note: The statements, opinions and data contained in all publications are solely those of the individual author(s) and contributor(s) and not of MDPI and/or the editor(s). MDPI and/or the editor(s) disclaim responsibility for any injury to people or property resulting from any ideas, methods, instructions or products referred to in the content.